A Computational Fluid Dynamics Analysis of a Driver-Assistive Truck Platooning System with Lateral Offset

by

Hugh Humphreys IV

A thesis submitted to the Graduate Faculty of
Auburn University
in partial fulfillment of the
requirements for the Degree of
Master of Science

Auburn, Alabama
May 6th, 2017

Keywords: Aerodynamics, Computational Fluid Dynamics, Autonomous Vehicles, Truck
Platooning, Fuel Economy

Approved by

Dr. D. Steven Nichols, Assistant Professor of Aerospace Engineering
Dr. David M. Bevly, Professor of Mechanical Engineering
Dr. David E. Scarborough, Assistant Professor of Aerospace Engineering

Abstract

This study utilizes Computational Fluid Dynamics to analyze the aerodynamic drag performance of a two-truck Driver-Assistive Truck Platooning system. Simulations were conducted to characterize the drag reduction versus separation distance trend for standard platooning from separation distances from 0-100 ft. From the CFD simulations, it was determined that the drag reduction monotonically increased as the separation distance diminished. Fuel economy tests were then conducted to compare the simulated results to practical experimental results. The follower truck's fuel economy improvement differed from the CFD predictions, and thus a new series of simulations were conducted to determine the impact of external platooning effects such as lateral offset and crosswind. These results were then compared to both the original CFD simulations, as well as fuel economy results and select wind tunnel results from various other groups. The CFD simulations of lateral offset demonstrated a significant degradation in the follower truck's savings, whilst the lead truck was mostly unaffected. CFD simulations also predict that crosswind also degrades the centered drag reduction trend for both vehicles, while also accentuating the degradation present in the lateral offset trends. This reduction in aerodynamic drag savings is also predicted to be directionally dependent for the lateral offset cases.

Acknowledgments

I would like to thank Dr. Batterson for starting me on the project and mentoring me throughout the process of this thesis, along with Dr. Bevly and everyone else who helped or supported me throughout this work.

Table of Contents

List of Tables

List of Abbreviations

DATP	Driver-Assistive Truck Platooning
ATRI	American Transportation Research Institute
GPS	Global Positioning Systems
LIDAR	Light Detection and Ranging
DOT	Department of Transportation
EPA	Environmental Protection Agency
CACC	Cooperative Adaptive Cruise Control
FHWA	Federal Highway Administration
EARP	Exploratory Advanced Research Program
ATRI	American Transportation Research Institute
ITS	Intelligent Transportation Systems
NREL	National Renewable Energy Laboratory
SAE	Society of Automotive Engineers
RANS	Reynolds-Averaged Navier Stokes
RKE	Realizable k-ε
TKE	Turbulent Kinetic Energy
CAD	Computer Aided Design
ROI	Region of Interest

Chapter 1
Introduction

This chapter introduces the problem of modeling the aerodynamics of a Driver-Assistive Truck Platooning (DATP) system. The goal of a platooning system is to reduce the fuel consumption of the vehicles by taking advantage of aerodynamic drag reductions through a phenomenon commonly referred to as drafting. DATP is achieved through a combination of sensors which allows the vehicles to be longitudinally controlled by an algorithm, rather than a driver. This decreases the response time of the system, allowing for drastically reduced following distances. Motivation for the work on DATP systems, and a review of previous work done in this area is included in this chapter to provide insight into various aspects of the problem.

1.1 Motivation

In 2014, the trucking and logistics industry represented approximately 8.3 percent of the annual gross domestic product in the United States [1]. Within this industry, trucking represents 68.9% of all value transported, comprising the dominant mode of transportation within the United States [2]. With sustained projected growth for the trucking industry moving forwards [2], companies in the transportation sector constantly seek ways to decrease cost in operating vehicles in order to increase profits.

Within the transportation industry, there has been a renewed focus on improvements in fuel economy. According to the American Transportation Research Institute (ATRI) fuel is the second highest operational expense in operating a fleet of commercial vehicles, behind only personnel costs [3]. This high operating cost is particularly detrimental to large fleets due to its highly

variable nature. The majority of heavy commercial vehicles in the United States operate on diesel fuel, a derivative of crude oil. Crude oil is traded as a global commodity, which in turn makes the price fluctuate based on supply and demand. This represents a highly variable cost input towards a trucking operation that is outside of the control of trucking companies. The impact is intensified by the rise of diesel prices over the past decade, as shown in Figure 1 [4]. With the price of diesel outside the companies' control, reducing the fuel consumed by heavy vehicles is highly desirable to limit operational costs within the company.
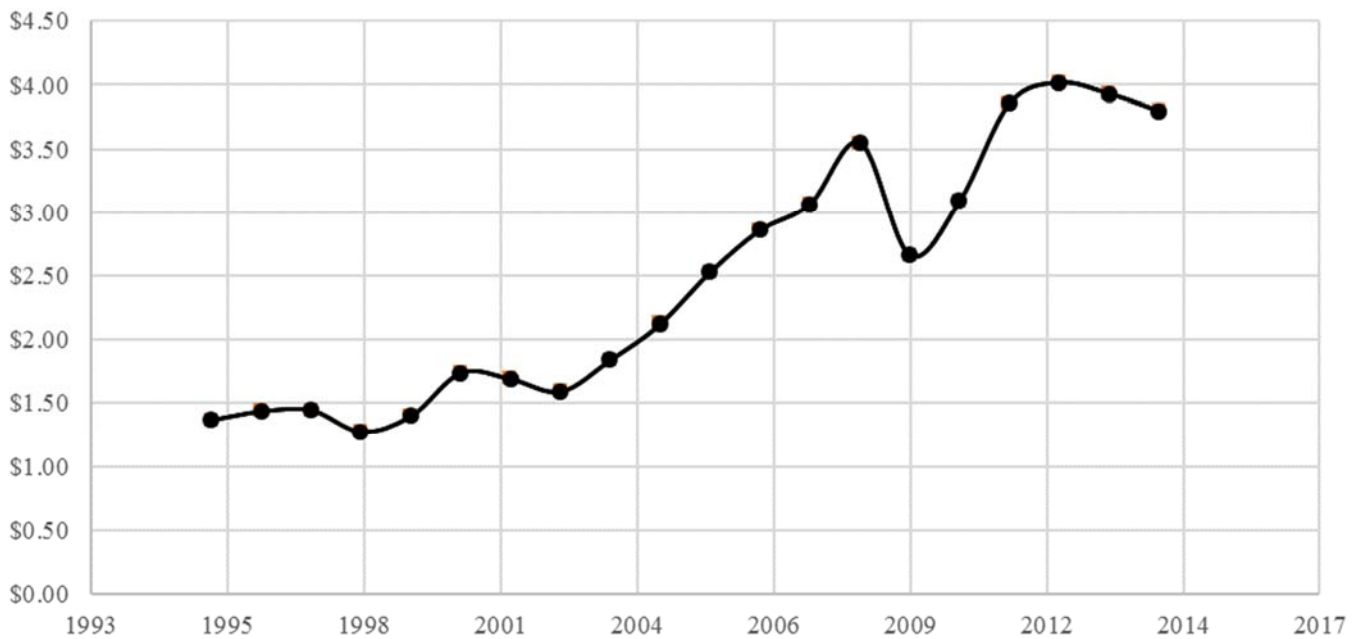
Figure 1: Annual No.2 Diesel Price for the United States [4]

The expense alone is sufficient motivation for reducing the amount of fuel consumed by heavy vehicles, but with growing national concern over the environmental impacts of the transportation industry, new federal regulations by the Department of Transportation (DOT) and Environmental Protection Agency (EPA) provide further incentives towards reducing fuel consumption. Reductions in fuel consumption provide a multitude of additional benefits which are potentially as valuable as the simple cost reduction. As companies seek to reduce their carbon

footprint, a reduction in the amount of fuel consumed provides an attractive alternative to gas suppression or filtering systems, as it reduces both emissions and fuel costs. The large scale of the trucking industry entails that even small percent reductions in the fuel consumed can have large ramifications for the industry.

The total overall losses present in an engine for heavy vehicles can be expressed in terms of four various sources: total drag, grade changes, power train losses, and accessory losses (e.g. air conditioning and electrical systems). The total drag, one of the dominant sources of fuel performance losses, is comprised of two parts as follows:

$$D = \underbrace{\frac{1}{2}\rho v^2 C_d A}_{\substack{\text{Aerodynamic} \\ \text{Drag}}} + \underbrace{F_n \mu_{rr}}_{\text{Rolling Resistance}} \tag{1.1}$$

Where D is the total drag, ρ is the density of the air, v is the velocity of the air, C_d is the coefficient of aerodynamic drag for the vehicle, A is the reference area for the vehicle, F_n is the normal force exerted by the vehicle, and μ_{rr} is the coefficient of rolling resistance. From Equation (1.1), it is evident that the aerodynamic drag's trend goes with the velocity squared, while there is no dependence on the velocity for the rolling resistance. Therefore, at highway velocities, the aerodynamic drag dominates the overall drag trend, typically comprising up to 65% of the total fuel consumption [5]. Additionally, the aerodynamic drag is directly proportional to the coefficient of drag, which depends on various physical parameters of the vehicle itself.

Tractor-trailer configurations of heavy vehicles, are characterized by their high positive pressure distributions on the front surfaces and negative pressure distributions on the rear surfaces typical of flow separation [6]. Thus, the primary source of aerodynamic drag comes from the pressure drag, rather than the viscous drag, as the large regions of separated flow and strong

3

positive pressure gradients contribute far more to the overall aerodynamic trend. When seeking to reduce the drag acting on a heavy vehicle, minimizing the pressure drag experienced serves as a good candidate for reducing the total aerodynamic drag experienced by the vehicle.

Throughout the United States, efforts to improve the fuel economy of heavy vehicles through aerodynamic improvements are evident. From Walmart's Advanced Vehicle [7] project and the Department of Energy's SuperTruck [8], to simpler advancements such as additions to the rear of the trailer [9], aerodynamic improvements to heavy vehicles are becoming extremely popular. The motivation for these aerodynamic improvements is twofold, a strong desire to reduce the fuel consumption of the vehicles coupled with improved tools for designing and evaluating the performance of proposed aerodynamic improvements.

Drafting is one effective way to diminish the drag experienced on a vehicle. Drafting reduces the pressure drag experienced on both vehicles in the drafting pair through two separate mechanisms. The lead vehicle typically sees drag reduction due to the follower truck's disruption of the flow field behind the lead truck. Positioned closely enough, the follower vehicle disrupts the recirculating flow behind the lead vehicle caused by the flow separating. This disruption increases the pressure distribution on the rear surface of the lead truck. Meanwhile, the velocities behind the lead truck are significantly lower than the free-stream flow. The follower truck, meanwhile, is slipped into the lower velocity airflow present behind the lead truck, which in turn decreases the pressure distribution on the front surfaces of the follower truck. Therefore, platooning potentially decreases the drag experiences by both vehicles, decreasing the fuel required to operate the vehicles and reducing costs to operators. Drafting is frequently used in a multitude of scenarios other than platooning, such as in NASCAR and cycling, where athletes utilize drafting to give themselves a competitive edge.

Prior to DATP, drafting was not previously seen in a highway scenario. Human reaction times make following at close separation distances without electronic aid extremely risky. The large masses involved with heavy vehicle transportation have previously made drafting vehicles infeasible. With a loaded trailer traveling at highway speeds, the required stopping distance in an emergency situation was much greater than the following distance required by the lead vehicle to see benefits. The primary limiting factor in this safety situation was the average reaction time of a human driver. Previous studies have concluded that the average time required for a driver to respond to a change in the road conditions was approximately 1.28 seconds for a full retraction of the throttle pedal, prior to the brake pedal even being depressed [10]. Under typical driving weight and speed of 65,000 lbs. and 65 mph, respectively, this translates to a stopping distance of over 300 feet [11]. With these safety concerns in mind, most states have litigation designed to limit risky driving behaviors, making drafting under normal circumstances illegal.

1.2 Current Work

In recent years, advances in sensing technology such as high resolution Global Positioning Systems (GPS) techniques, and cost reductions in Light Detection and Ranging (LIDAR) systems have moved autonomous vehicles from science fiction to a near-term deployment scenario. The DATP prototype analyzed in this study builds upon existing Cooperative Adaptive Cruise Control (CACC) technologies to reduce the reaction time of the system. The DATP system utilizes radar and Dynamic-base Real Time Kinematic (D-RTK) GPS for redundant ranging measurement, coupled with Dedicated Short Range Communications (DSRC) for communication between the vehicles. This enables the paired trucks to respond significantly faster than a human driver is capable of responding, enabling shorter separation distances than would be possible for a human

driver while maintaining a safe margin [12]. Overall, this reduces the response time of the follower truck to braking situations initiated by the front truck on the order of milliseconds. This drastic decrease in the response time of the system enables extremely close following distances. The lead truck in the platooning pair is still completely controlled by a human driver, and the following truck's lateral control is still the responsibility of a human driver thus classifying the system as an SAE Level 1 autonomous system [13].

In addition to controlling the follower truck's brake and throttle, the DATP system also provides the follower truck driver with a video link displaying the road conditions in front of the lead truck. This allows for greater response time in the case of a failure of the system, giving the driver of the follower truck more time to react to any unforeseen situation. These improvements make drafting of heavy vehicles a possibility, and thus the Federal Highway Administration (FHWA) has stated as part of the Exploratory Advanced Research Program (EARP) that systems providing any level of vehicle automation are of high research and commercial value [14].

Auburn University, together with partners Peterbilt Trucks, Peloton Technology, and the American Transportation Research Institute (ATRI) proposed and was awarded a contract to analyze various aspects of DATP systems regarding their near term-viability. Among many of the concerns highlighted by the project is accurately quantifying the fuel savings that a DATP system provides. Since the aerodynamic drag is inherently linked to the fuel consumption, understanding the drag reduction offered by DATP systems is paramount to understanding the cost-benefit of a DATP system.

As part of the overall project, numerical simulations were conducted to characterize the drag reduction trend with regards to following distance [15]. In order to determine the drag experienced by the vehicle, many characteristics of the flow field surrounding the vehicles is required.

Numerical simulations are advantageous in this scenario due to their high flexibility and low cost when compared to traditional experimentation. The most relevant parameters in regard to numerical simulation are the hardware requirements, software pricing and analysis time. Wind tunnel testing is less flexible in the number of scenarios that can be tested for a given desired cost as new scenarios potentially require new hardware or other costly changes. This is exacerbated by the requisite length scale of the problem under consideration, as elimination of wall effects requires significant consideration [16,17].

Practical experimentation is also extremely cost-prohibitive, as directly determining the pressure field around the trucks would require an unaffordable number of sensors. Indirect measurements of the drag experienced by the vehicles, such as fuel economy tests, require additional resources and add the additional challenge of isolating the aerodynamic effects from other variables inherent to operating heavy vehicles at highway speeds. Combining varied numerical simulations with specific practical experimentation as validation provides a well-balanced tradeoff yielding robust results with high confidence. Therefore, as part of the project, ANSYS's CFD package FLUENT was used as the primary analysis tool [18]. Supplementing the numerical analysis, was an SAE Type II Fuel Economy test, where two Peterbilt 579's were tested using Peloton's DATP prototype [19].

1.3 Existing Literature

Several previous studies analyzing the effect of platooning in regards to the fuel economy gains have been conducted in previous years. Computational studies rely on well-constructed experimental studies for validation. Vehicles in a platooning configuration are not well-represented in the literature for experimental results that directly measure the aerodynamic forces.

Despite this, there has been significant work on simplified blunt bodies that model the flow around vehicles. Therefore, in order to build confidence in the turbulence and meshing scheme, generic bluff bodies known as Ahmed Bodies were modeled for this project [20].

The Ahmed body has become a standard for validating computational studies in the automotive industry, as it is understood to well-represent the aerodynamic characteristics of vehicle bodies [21,22]. Additionally, the Ahmed body is particularly useful for the study conducted due to Pagliarella's work [23] which analyzed two Ahmed bodies in tandem by varying the separation distance. The work conducted by Pagliarella is highly valuable to the simulation effort because the results are normalized by the single body drag and reported for various separation distances. Therefore, the results can be used as "truth" for comparing to the simulated aerodynamic drag coefficient.

Additionally, several groups previously conducted fuel economy tests for heavy vehicle platooning, although nearly all of them provide challenges when used for validation. Bonnet and Fritz performed platoon tests using loaded tractor-trailers at low speeds with a small range of separation distances [24]. Comparisons between the studies are further complicated due to the difference in geometries, where Bonnet and Fritz utilized the DaimlerChrysler ACTROS as the model for the vehicles. The fundamental shape of the tractor is more similar to vehicles common in Europe, but less common in the United States. The European style vehicles are sufficiently different aerodynamically, with a much flatter front surface of the tractor, and thus they exhibit different flow characteristics over the tractor. Two examples typical of the differences between a European style cab versus the tested Peterbilt 579 is shown in Figure 2.

Figure 2: (Left) American Cab Peterbilt 579   *(Right) European Mercedes Benz Acturos*

Similar to these tests, the Energy Intelligent Transportation Systems (ITS) program in Japan also reported fuel economy results [25]. These tests need to be heavily qualified in context, as they utilize unloaded trailers where the offset was tightly controlled via a physical connection. Furthermore, California's Partners for Advanced Transportation Technology (PATH) program conducted wind tunnel testing on subscale models of platooned tractor-trailer configurations [26] The general consensus amongst the previous research is that the drag reduction increases as the separation distance diminishes.

Recently, there have been several other fuel economy tests conducted. Tests conducted by the National Renewable Energy Laboratory (NREL) [27] utilized an early version of Peloton's DATP system [28] to conduct a Society of Automotive Engineers (SAE) Type II fuel economy test [19]. The SAE Type II fuel economy test is the current standard accepted by the automotive industry for accurate measurement of fuel economy improvements. While fuel economy measurements always provide a challenge in extricating the aerodynamic trends from the inherent losses associated with traveling on highway, the aerodynamic drag represents the largest portion

9

of the drag acting on the vehicles, and thus it can be assumed that the fuel consumption trend tracks well with the aerodynamic drag trend.

There is a large deficit of work comprising an in-depth study into the drag reduction versus separation distance trend developed for a DATP system. This thesis attempts to characterize this trend, and compare it to experimental data for validation. The following chapter describes the fundamental background theory involved in the simulation of the vehicles.

Chapter 2

CFD Background Theory and Methodology

The goal of CFD analysis is to solve the fundamental governing equations of fluid dynamics, namely the Navier-Stokes equations, in order to determine parameters such as the density and velocity of the local flow. These variables are important to determine more general parameters such as the drag force acting on the vehicles. The steps required to accomplish this goal are outlined in this section.

2.1 Methodology

For CFD analysis, 3D geometry must be constructed for each of the test models. To accomplish this, the popular Computer Aided Design (CAD) software SolidWorks, made by Dassault Systems was utilized [29]. Nearly any CAD software would have sufficed, but SolidWorks was chosen due to its existing geometry interface with ANSYS's DesignModeler, the geometry precursor to the fluid mechanics solver, FLUENT. In addition, since SolidWorks is a popular choice within the industry, there was a wealth of informational services for reference for this thesis [30]. After construction of the primary geometry in SolidWorks, the 3D geometry was then imported into the DesignModeler Software for preparation for the Meshing Software present in ANSYS's fluid mechanics package. There, several small additions were made to the geometry, mainly shapes generated to perform mesh refinements in the meshing software.

Mesh refinements were essential for accurately modeling the wake structure behind both the simplified Ahmed bodies, as well as the complex tractor-trailer geometries. The length scales between the relatively simple free-stream flow in front of the tractor-trailer, and the turbulent wake structures behind the vehicles requires different levels of refinement in the mesh.

In prior work, two different turbulence models were compared for their accuracy in capturing the wake structure behind the vehicles [15]. A Reynolds Averaged Navier-Stokes (RANS) approach and a Detached Eddy Simulation (DES) approach were selected as candidates for the analysis of heavy platooning due to computational efficiency and prevalence in previous CFD analyses. The following section outlines the fundamental background theory regarding the computational process, as well as the turbulence model selected.

2.2 CFD Theoretical Overview

The goal of the study was to characterize the drag reduction trend in regards to the separation distance. To accomplish this, the drag must be calculated from the following equation:

$$F_D = \frac{1}{2} C_D \rho_\infty V_\infty A \tag{2.1}$$

where C_D is the coefficient of aerodynamic drag, ρ_∞ is the free-stream density, V_∞ is the free-stream velocity, and A is the reference area. As seen in the above equation, the drag force then depends on the coefficient of aerodynamic drag. This is a property that depends on the local properties of the flow. Therefore, the local properties of the vehicles must be determined.

In general, these properties can be determined through the Navier-Stokes equations, which are comprised of expressions for conservation of mass and conservation of momentum, which are shown in Equation (2.2) and Equation (2.3) [31].

$$\frac{\partial p}{\partial t} + \nabla \cdot (\rho \bar{v}) = S_m \tag{2.2}$$

$$\frac{\partial}{\partial t}(\rho \bar{v}) + \nabla \cdot (\rho \bar{v}) \bar{v} = -\nabla p + \nabla \cdot (\bar{\tau}) + \rho \bar{g} + \bar{F} \tag{2.3}$$

where

$$\rho \quad = \quad \text{Density}$$

$$t \quad = \quad \text{Time}$$

$$\bar{v} \quad = \quad \text{Velocity}$$

$$S_m \quad = \quad \text{Mass Source Term}$$

$$p \quad = \quad \text{Pressure}$$

$$\bar{g} \quad = \quad \text{Gravitational Acceleration}$$

$$\bar{F} \quad = \quad \text{Body Forces}$$

$$\bar{\tau} \quad = \quad \text{Stress Tensor}$$

Combined with an equation of state and conservation of energy, shown in Equations (2.4) and (2.5), respectively, these equations fully define any non-reacting fluid flow field [31].

$$p = \rho RT \tag{2.4}$$

$$\frac{\partial}{\partial t}(\rho E) + \nabla \cdot \left(\bar{v}(\rho E + p) \right) = \nabla \cdot \left(k_{eff} \nabla T - \sum_j h_j \bar{J}_j + \left(\bar{\tau}_{eff} \cdot \bar{v} \right) \right) + S_h \tag{2.5}$$

where

$$E \quad = \text{Energy}$$

$$\rho \quad = \text{Density}$$

$$T \quad = \text{Temperature}$$

$$k_{eff} \quad = \text{Effective Conductivity}$$

$$h_j \quad = \text{Sensible Enthalpy}$$

$$S_h \quad = \text{Volumetric Heat Source}$$

These equations have no closed-form analytical solution for a generalized case, with only a select few highly-simplified boundary conditions having direct analytical solutions. Therefore, numerical discretization is utilized to approximate the solution to Equations (2.2) and (2.3).

There are many software packages that will perform the required iterative solution process. For the purposes of this investigation, ANSYS Inc.'s FLUENT was used [18]. Flow surrounding heavy vehicles is relatively low speed, with very little compressibility and almost no heat transfer, with high turbulence. Since the density is relatively constant and there is no heat transfer, the energy equation contributes relatively little information to the system of equations, and thus it is not necessary to include an energy equation model. Additionally, an unstructured mesh was a relatively strict requirement of the software package, due to the complex nature of the modeled geometry. Attempting to construct a structured mesh surrounding the many curves of the vehicles proves a prohibitive task. Therefore, FLUENT served as an ideal choice due to its large number of turbulence models, as well as the capability to solve an unstructured mesh.

FLUENT utilizes conservation of mass, Equation (2.2), and conservation of momentum, Equation (2.3) combined, usually referred to as the Navier-Stokes equations, in order to generate a system of equations to resolve the flow properties . Equation (2.6) presents the generalized form of the conservation equations [31]. Here, ϕ represents the quantity to be transported with respect to the mass.

$$\int_V \frac{\partial \rho \phi}{\partial t} + \oint \rho \phi v \cdot d\overline{A} = \oint \Gamma_\phi \nabla_\phi \cdot d\overline{A} + \oint S_\phi dV \qquad (2.6)$$

For the continuity equation, ϕ represents $\dfrac{\partial m}{\partial m} = 1$, and for the momentum equation, ϕ is

$\dfrac{\partial(mv)}{\partial m} = v$. Substituting these relations into Eq. (2.6) yields the following for the continuity and

momentum equation, respectively.

$$\int_V \frac{\partial \rho}{\partial t} + \oint \rho v \cdot d\bar{A} = \oint \Gamma_\phi \nabla_\phi \cdot d\bar{A} + \oint S_\phi dV \tag{2.7}$$

$$\int_V \frac{\partial \rho v}{\partial t} + \oint \rho v^2 \cdot d\bar{A} = \oint \Gamma_\phi \nabla_\phi \cdot d\bar{A} + \oint S_\phi dV \tag{2.8}$$

Once Equations (2.7) and (2.8) are discretized, there are then two different traditional approaches to solving Equations (2.7)and (2.8). The first is a density based approach. In the density based approach, continuity, momentum and the energy equation are coupled together and solved simultaneously. In the density based approach, the continuity equation is used to determine the velocity field, and then the pressure field is determined from the equation of state. Traditionally, this yields fast convergence for high-speed flows where the density field changes rapidly throughout the domain.

The alternative to a density-based solution is a pressure based solution. Pressure based solutions come in both segregated and coupled forms, where the segregated solution yields slower convergence while yielding lower memory requirements. Figure 3 shows an overview of the algorithmic steps undertaken to obtain a solution in the coupled algorithm, which was used for all the simulations, for reasons explained in the next paragraph.
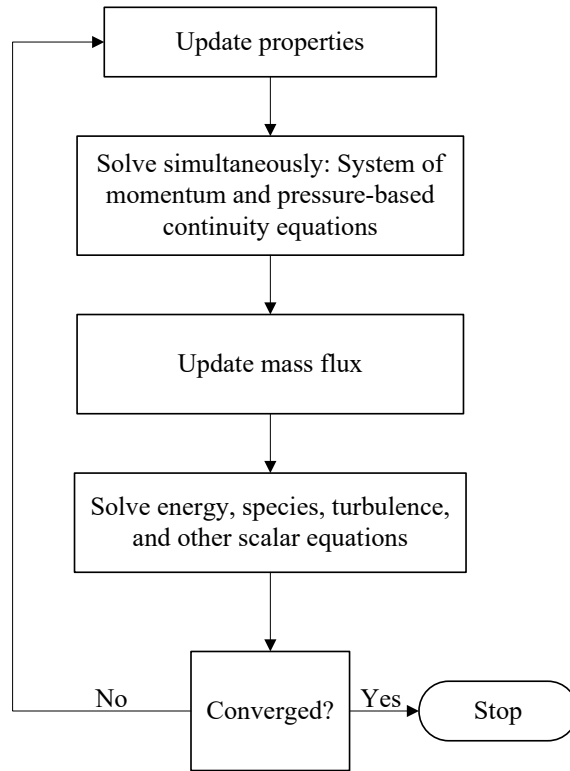
Figure 3: Overview of coupled pressure-based algorithm [31]

The coupled algorithm is significantly faster at achieving convergence than its segregated counterpart, since the system is solved simultaneously. However, this increased convergence speed comes at the cost of memory consumption, since the entire system of momentum and pressure-based continuity equations is stored in memory rather than the segregated algorithm's single equations method. The pressure-based solution varies from the density based solution, as the mass flux is isolated from the pressure based continuity and momentum equations. After determining the solution of the pressure field from a pressure-correction equation, the density field is determined from the continuity equation, and then the mass flux is determined. This typically yields extremely fast convergence in low speed, incompressible flows. Since the vehicles are low speed, (less than Mach 0.3) and the flow is relatively incompressible the coupled-pressure based solution was used for all simulations.

After discretization, the resulting system is linear. Both the momentum and continuity transported equations, once discretized, can be written via their residual form as per Equation (2.9).

$$\sum_{j}[A]_{ij}\,\overrightarrow{X_j} = \overrightarrow{B_i} \tag{2.9}$$

where $[A]_{ij}$ is the coefficient matrix with i and j representing the influence of neighboring cells in spatial directions. The residual matrix, $\overrightarrow{B_i}$ and unknown matrix $\overrightarrow{X_j}$ are both vectors of the form:

$$\overrightarrow{X_j} = \begin{bmatrix} p_i' \\ u_i' \\ v_i' \\ w_i' \end{bmatrix}; \quad \overrightarrow{B_i} = \begin{bmatrix} -r_i^p \\ -r_i^u \\ -r_i^v \\ -r_i^w \end{bmatrix} \tag{2.10}$$

Equation (2.9) is then solved iteratively using the coupled Algebraic MultiGrid (AMG) solver, which is suitable for large sparse matrices. The AMG within FLUENT is ideal for these types of matrices since they solve solution systems with N unknowns with only $O(N)$ work, and can be parallelized to take advantage of modern hardware [31].

This solution process can be accelerated through the use of appropriate relaxation factors. When working towards convergence, relaxation factors help reduce the time required for convergence by accounting for the true nonlinearity present in the Navier-Stokes equations even within the linearized equations. Through the addition of a new correction term, the property's predicted value is altered through the addition of a user-specified growth factor, so that the solution does not "overshoot" the correct value.

2.3 Realizable k-ε Turbulence Model

For the RANS model, a two-equation turbulence model was chosen due to its prevalence in vehicle aerodynamic analysis. The RANS model of choice for the work conducted in this thesis was the Realizable k-ε (RKE) model. The RKE model is a variation upon the standard k-ε model, first developed by Launder and Spalding [32]. It's primary enhancement to the standard k-ε model is to change the way the turbulent dissipation is handled. Other traditional k-ε models in the past have failed to accurately predict turbulent features in flows that have strong streamline curvature and rotation [31]. Since the flow surrounding the vehicles contains many of the features for which standard k-ε models improperly predict properties, the realizable k-ε model serves as a good choice.

The realizable k-ε model handles the introduction of the Reynolds stresses through two additional terms. The first is "k", the turbulent kinetic energy (TKE), which is defined via the definition of massless kinetic energy, Equation (2.11).

$$k \equiv \frac{1}{2}\left(\overline{u'u'} + \overline{v'v'} + \overline{w'w'}\right) \tag{2.11}$$

The second of the additional terms, "ε", is defined as the rate of dissipation of k due to viscous stresses, and is defined in Equation (2.12).

$$\varepsilon \equiv \nu \overline{\frac{\partial v_i'}{\partial x_k}\frac{\partial v_i}{\partial x_k}} \tag{2.12}$$

These new terms are then related to the Reynolds stresses mentioned above via the Boussinesq hypothesis which relates the mean velocity gradients to the Reynolds stresses [33].

$$-\rho\overline{u_i'u_j'} = \mu_t\left(\frac{\partial u_i}{\partial x_j} + \frac{\partial u_j}{\partial x_i}\right) - \frac{2}{3}\left(\rho k + \mu_t\frac{\partial u_k}{\partial x_k}\right)\delta_{ij} \tag{2.13}$$

Solving these additional equations yields equations that serve to model turbulence introduced into the flow. While the RKE model works extremely well for the vast majority of the flow regime, near the wall the RKE method fails to capture non-trivial aspects of the flow that occur in the viscosity dominated region of the near-wall. Therefore, a secondary model is typically used to resolve the flow near the wall. For the purpose of this work, the standard wall function from FLUENT, an empirical model first developed by Launder and Spalding, is utilized to determine the velocity in the boundary layer near the wall, shown in Equation (2.14) [32].

$$U^* = \frac{1}{\kappa} \ln\left(Ey^*\right) \tag{2.14}$$

where:

U^* = Dimensionless mean velocity

κ = von Kármán constant = 0.4187

E = Empirical constant = 9.793

y^* = Dimensionless distance from wall

This approach relies on the assumption that the wall is at equilibrium, which is usually a valid assumption. Under strong pressure gradients however, this equilibrium assumption breaks down, and an additional treatment is required near the wall in order to properly account for the effects of these pressure gradients. Since the regions surrounding the vehicles which are essentially bluff bodies exhibit these strong pressure gradients, a modification to the standard wall-function is required. A non-equilibrium approach designed to capture the effects of a spatially dependent pressure field was developed by Kim in 1995 [34]. The log-law relationship shown in Eq. (2.14) is then modified to become:

$$\frac{\tilde{U}C_\mu^{0.25}k^{0.5}}{\mu_t^2} = \frac{1}{\kappa}\ln\left(E\frac{\rho C_\mu^{0.25}k^{0.5}y}{\mu}\right) \quad (2.15)$$

Equation (2.15) is then used to determine the TKE, which allows it to be used throughout the whole domain, except in cells directly at the wall, where a zero TKE production boundary condition is applied, which is implemented using Equation (2.16).

$$\frac{\partial k}{\partial n} = 0 \quad (2.16)$$

These models then are used for the entirety of the solution process throughout this thesis. More in-depth information regarding the overall solution process, including a full derivation of the equations shown can be found in the ANSYS FLUENT theory guide [31]. With the background theory developed, the following chapters describe the simulation setup and discuss the results.

Chapter 3

Two Truck Simulation Methodology and Results

The following section details the results of the initial two truck analyses. The majority of the presented analysis in this chapter was conducted by prior research [15]. However, a summary of the previous work conducted is necessary before presenting modifications of made under this thesis, and thus a summary of the more important results from the previous work along with the author's contributions and enhancements of the current work are presented in this chapter.

3.1 Grid Refinements and Validation

In general, it is a good practice to simulate generic models with well understood aerodynamic properties to build confidence in the numerical model. The generic model, while not directly related to the problem at hand, helps to verify that the modeling choices selected accurately capture the desired physical effects. Within the existing literature, there is an absence of well-validated experimental tractor-trailer data, particularly when platooned, and therefore, a generic body which well-represented the aerodynamic characteristics of a vehicle was selected for a validation case. The chosen body is commonly referred to as the Ahmed body, and is comprised of a simplified car geometry which captures the aerodynamic impacts of a vehicle, particularly in the wake region, depicted in Figure 4.
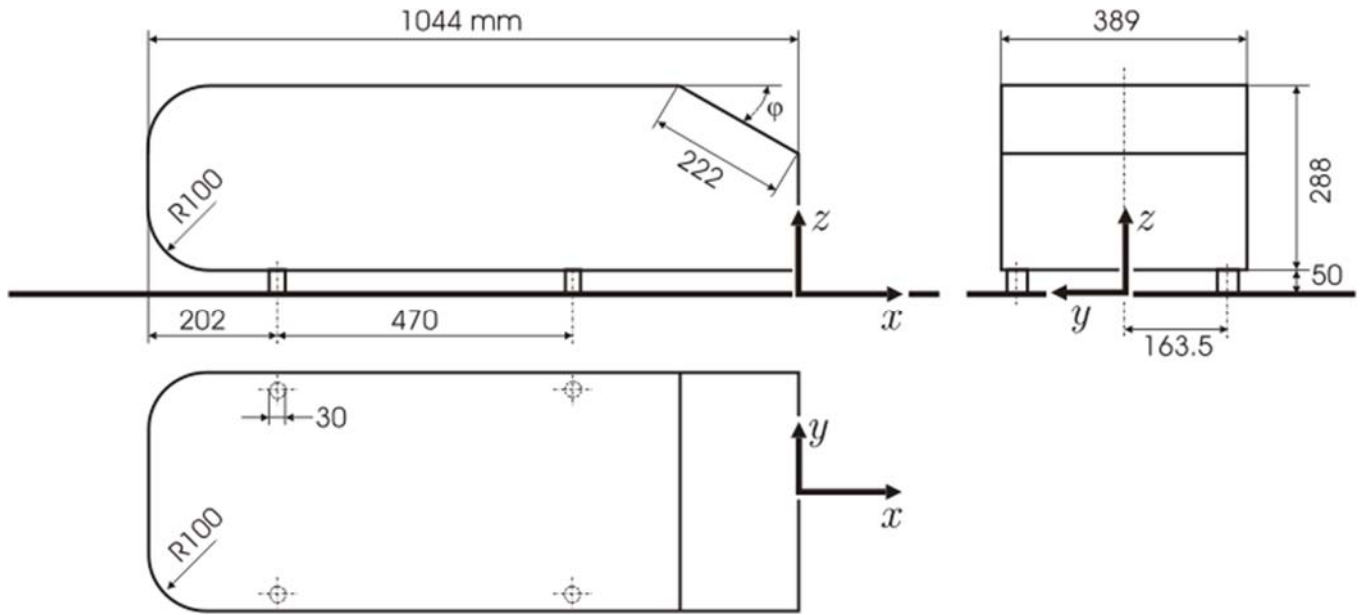
Figure 4: Schematic of Ahmed Body [20]

The Ahmed body's aerodynamic properties were first determined via wind tunnel testing in 1984 by Ahmed [20]. Since then, it has become a common validation tool for numerical studies [35,36]. Comparing the results from numerical simulations to the wind tunnel measurements provides valuable confirmation that the meshing and turbulence schemes employed can capture the physics present in the problem.

Within the paper previously discussed by Ahmed, two different bodies were considered, one with a slanted rear face, and one flat across the back. Since typical tractor trailers more closely resemble the flat, rather than the sloped Ahmed body, the flat model was selected for validation despite Pagliarella's work which primarily included sloped Ahmed bodies [20,23]. Using this as a metric, a non-traditional grid-independence study was conducted, where the relative error in the computed coefficient of drag for the platooned Ahmed bodies was compared to the result achieved by Pagliarella's group. A plot showing the results from this investigation are shown in Figure 5.
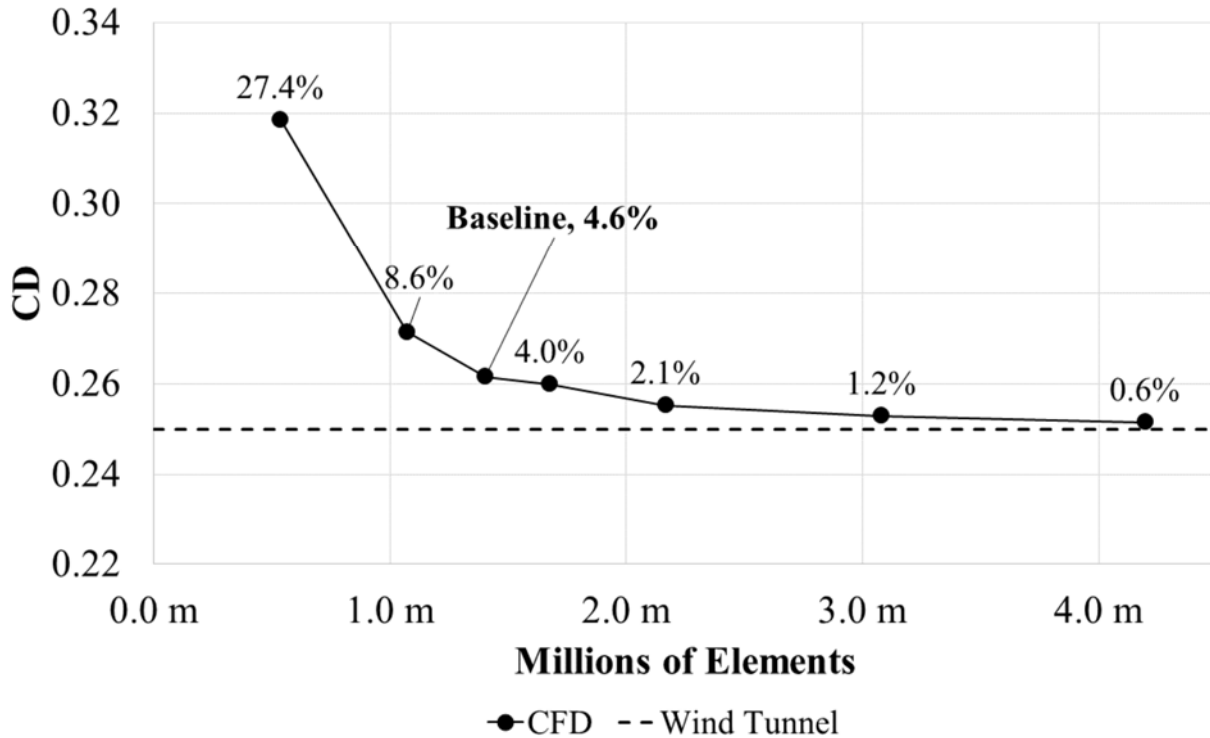
Figure 5: Single Ahmed body coefficient of drag vs. millions of elements [15]

Traditionally, grid independence is investigated iteratively through extending the Region of Interest (ROI), which is the total simulated control volume, including the body being simulated, as well as its enclosure. A simulation which has received sufficient grid refinement and properly established boundary conditions then demonstrates a sufficiently small difference as the ROI is extended, and thus confidence that the bodies of interest are modeled properly is established. Since grid independence is not an absolute, but rather an acceptable tolerance, a relative error of approximately 5% was deemed sufficient, since the marginal benefit of adding further elements is greatly diminished past this point, which can be seen in Figure 5, along with a significantly larger marginal increase in computational time.

Additionally, larger mesh sizes, while possible for single bodies, would rapidly become impractical for the platooned scenarios where the appropriate mesh sizing for extremely accurate

values in the single-body scenario would rapidly lead to hardware limitations. Typically, in CFD simulations, the goal is to drive the estimated error in the solution as close to zero as possible. Reduction in the error of the simulations is achieved through an increase in the number of elements, which thereby decreases the error in the numerical approximation, while increasing the computational time required to solve the simulation.

Since the Ahmed body is being modeled as a validation case, one of the goals in the study of the Ahmed body was to keep as many of the parameters in the meshing and simulation of the Ahmed body like that of the truck simulations. Therefore, accuracy levels that could be achieved for the Ahmed body by adding more meshing elements, or decreasing the convergence criteria may not be sustainable in multiple platooned heavy vehicle simulations due to the hardware and time constraints. Thus, to remain consistent in the simulations across the single body and platooned bodies, the acceptable level of error was deemed significantly higher than would be acceptable if only a single body case was chosen. With these constraints in mind, Table 3-1 summarizes the key components of the global meshing parameters used in the modeling of the Ahmed Body.

Table 3-1: Ahmed body simulation global meshing parameters [15]

Parameter	Value
Advanced Sizing	Proximity and Curvature
Smoothing	High
Minimum Cell Size	1mm
Max Face Size	250mm
Max Size	250mm
Growth Rate	1.2

Surface Meshing	
Location	Sizing (mm)
Body	10
Legs	2

In addition to the global meshing parameters, the flow surrounding the vehicles has relatively sharp gradients which cause dramatic changes in the flow's properties. In the far-field, where these gradients are small, the relatively large elements generated through the global meshing parameters are sufficient. Close to the vehicle however, additional refinement is necessary to ensure that there are enough volume elements to capture the large changes over a short distance. For the Ahmed body specifically, Watts developed three different refinement regions which are shown in Figure 6 [15].
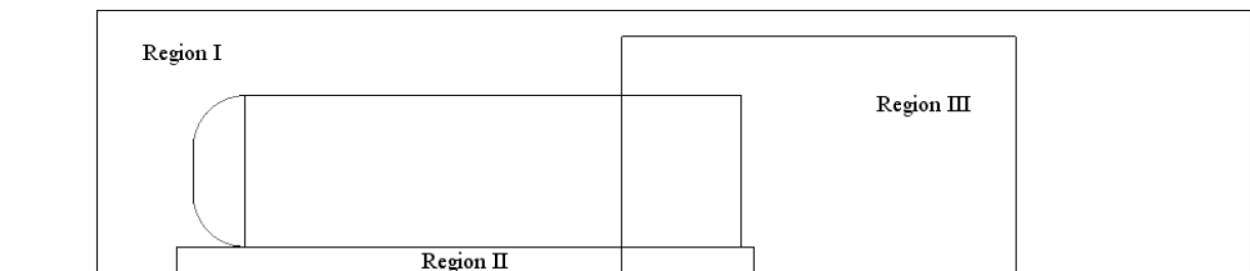
Figure 6: Refinement region for Ahmed body [15]

These enhanced regions each have different sets of meshing parameters based on the expected flow regime within each. Region 1 represents the region immediately surrounding the body, yet not within the far-field. This region serves to provide a slightly more refined mesh where the initial property gradients develop over the body, without the extreme sophistication in some of the wake zones. Region II represents the underbody area between the body and the simulated road.

This region is intended to capture the additional effects introduced by the body's "legs", as well as the relatively small length scale between the body and the road, comprising only 50mm, which is significantly smaller than the global meshing parameters. These two extra influences require a tighter mesh sizing to accurately capture the flow's properties in this region. Region III represents the wake region behind the vehicle. This region requires additional refinement to properly resolve the vortices and pressure fields behind the vehicle, which are significantly more complex than the interactions in Region I, due to the turbulence inherent in these structures. Table 3-2 summarizes the preferred sizes for each of these regions.

Table 3-2: Ahmed body refinement regions

Location	Preferred Size (mm)
Region I	30
Region II	15
Region III	20

In addition to the surface region refinements and volumetric region refinements, an additional modification must be made to the mesh cells near the body to account for the boundary layer. Within FLUENT, a special type of refinement is used to ensure that the element's faces are as normal to the body as is possible, called an inflation layer. This helps eliminate numerical artifacts that are caused by boundary conditions which must be satisfied at an angle. Within FLUENT these inflation layers are added as semi-structured elements, typically quadrilateral prismatic elements. These inflation layers are used within all the models along the surfaces of both the bodies and the simulated roads.

One common way to define these inflation layers is through the usage of a "First Aspect Ratio" method, where the growth ratio and number of layers is specified which thus defines the

maximum amount of growth between each layer. If chosen correctly, this method then minimizes the gradient of the volume change during the transition from the surface body elements through the structured prismatic inflation layer elements and into unstructured tetrahedral volume elements. The values for these parameters used in both the validation Ahmed body case, as well as the two-truck simulations were taken from the Best Practices Guidelines for Automotive External Aerodynamics in FLUENT, and are summarized in Table 3-3[37].

Table 3-3: Ahmed body inflation layer parameter values

Parameter	Value
First Aspect Ratio	5
Maximum Layers	5
Growth Rate	1.2

3.2 Solution Methods and Controls

After meshing, the single Ahmed body was then ready for simulation in FLUENT. The solution methods discussed in Section 2 were used throughout the entirety of the simulation process. These are summarized in Table 3-4. Additionally, when properly configured, relaxation parameters have no influence on the result of the final solution at convergence. Despite this, the relaxation parameters throughout the simulations were held constant to doubly ensure that no variations between runs was caused due to the solution setup.

Table 3-4: Solution methods for Ahmed body and relaxation factors

Solution Variable	Method
Pressure	Standard
Pressure-Velocity Coupling	Coupled
Momentum	SOU
Turbulent Kinetic Energy (k)	SOU
Turbulent Dissipation Rate (ε)	SOU
Relaxation Parameters	
Courant Number	50
Momentum Explicit Factor	0.25
Pressure Explicit Factor	0.25
Density Implicit Factor	1
Body Forces Implicit Factor	1
TKE Implicit Factor	0.8
Turbulent Dissipation Implicit Factor	0.8
Turbulent Viscosity Implicit Factor	0.95

The next phase of the simulation was to define the boundary conditions for the simulated control volume. Since the flow is incompressible, a simple velocity inlet condition, coupled with a description of the two transported turbulence variables (k and ε) is sufficient to fully define the incoming flow. Specifying the inlet velocity is a simple task for the models tested, since the velocity vector is fully normal to the front surface of the control volume's box. The outlet is then modeled in a typical fashion, a pressure-outlet set to zero-gauge pressure. In the modeling and

meshing portions of this thesis, the control volume was constructed in such a way that the rear surface would be sufficiently downstream to ensure a freestream pressure value. Therefore, the gauge pressure at the outlet can be reasonably assumed to be nonexistent.

For the bodies themselves, the solid bodies of interest within the flow were specified as "wall" type boundaries, which is used within FLUENT very specifically as a boundary through which no mass can penetrate, and a no-slip condition is enforced. Along the side walls and top of the overall control volume, a symmetry condition was applied. Within FLUENT, a symmetry condition indicates that there is a solid boundary which mass cannot penetrate once again. Unlike the wall boundary condition which enforces this through a zero-velocity condition, the symmetry condition enforces this zero-mass flux through a zero-shear condition. This is an acceptable condition for application in the far-field region, and thus serves as the outer walls of the control volume.

Once all conditions have been applied, a practical convergence criterion must be chosen. For many CFD problems this is handled through the continuity residual. This is generally the slowest residual to converge, yet is the most meaningful in many flows since the mass balance is of high importance. In this thesis, however, the quantity of interest is the coefficient of drag on the vehicles. Therefore, the most useful convergence criteria would be ensuring that the body forces calculated across the bodies has converged. While the continuity residual is closely correlated with the convergence of the body forces, it is possible that the body forces may still be in flux even with an otherwise converged continuity residual. FLUENT, however, is not capable of specifying a convergence criteria based on the calculation of the body forces. Thus, the simulations were deemed converged when the coefficient of drag remained constant within five significant digits through a minimum of 100 solution iterations, or 2000 iterations were completed, whichever was

29

shorter. Throughout testing, most of the simulations did not require the maximum number of iterations to satisfy this convergence criterion.

3.3 Reference Parameters

As stated previously, the goal of this thesis, as well as previous work was to characterize the drag reduction trend versus the separation distance [15]. Therefore, after determining the flow field across the vehicles, FLUENT calculates the coefficient of drag via Equation (2.1), repeated below.

$$F_D = \frac{1}{2} C_d \, \rho_\infty v_\infty^{\,2} A \qquad (3.1)$$

Thus, once the body forces have been calculated on the body of the vehicles, the coefficient of drag can be determined by rearranging the above equation as shown below:

$$C_d = \frac{2F_D}{\rho_\infty v_\infty^{\,2} A} \qquad (3.2)$$

FLUENT's determination of the coefficient of drag is dependent on the reference values for the freestream velocity, freestream density, and reference area. These are values that must be defined by the user to determine the coefficient of drag. Throughout the testing, the reference velocity was held constant at 30 m/s (67.1 mph) which is close to typical operational speeds of heavy vehicles on highways. While this varies from Ahmed's compared wind tunnel test of 40 m/s [20,15], the results are still comparable, since the coefficient of drag is nondimensionalized by the free stream velocity, under the assumption that the flow regime is not significantly different. Similarly, the density used through all simulations was the standard sea-level density for air, 1.225 kg/m³, which is once again comparable since the flow is considered incompressible. Finally, the reference area for the drag coefficient is the projected frontal cross section, which corresponds to 0.115032 m² for the Ahmed body. This value, by necessity of the changing geometry, was

calculated through FLUENT's projected area calculation tool for each separate body present in the simulation.

3.4 Ahmed Body Validation

After obtaining results for the coefficient of drag of a single Ahmed body, these results were then compared with the reported wind tunnel data considered as the "true" value for the Ahmed body. Once again, for the reasons outlined in the chapter's introduction, an error margin of less than 5% was deemed acceptable to keep future simulations both consistent with the modeling scheme, as well as computationally feasible given the hardware limitations.

With confidence in the single Ahmed body simulation established through comparison with Ahmed's original wind tunnel data, [20,15] the next step in the validation process incorporated modeling two Ahmed bodies in a platooning configuration, and comparing the computational results to the work done by Pagliarella [23]. Wind tunnel tests for platooned bodies serve as an invaluable resource for building confidence that the simulated models accurately capture all the effects present in the flow field.

Once again, with the goal of remaining consistent with previous runs, the meshing parameters, solution parameters, boundary conditions, and convergence criteria all remained the same to ensure cross-run comparisons. To capture the coefficient of drag trend versus the separation distance, the Ahmed bodies were simulated at separation distances from 0.05 meters to 2 meters, or 5% to 200% body-length. Table 3-5 shows all the distances simulated for the platooned Ahmed bodies [15].

Table 3-5: Platooned Ahmed body separation distances [15]

Separation Distance (m)	Percent Body Length
0.05	5%
0.15	15%
0.25	25%
0.50	50%
1.00	100%
1.50	150%
2.00	200%

After completing the test campaign for all distances, the resulting coefficients of drag for each vehicle versus the separation distance were plotted, and compared to the wind tunnel data generated by Pagliarella for comparison [23,15]. The data was normalized against a single Ahmed body, and thus a normalized coefficient of 1 represented no net change in the drag experienced by the body, when compared to a body not in a platooning configuration. This plot comparing the two results is shown in Figure 7.
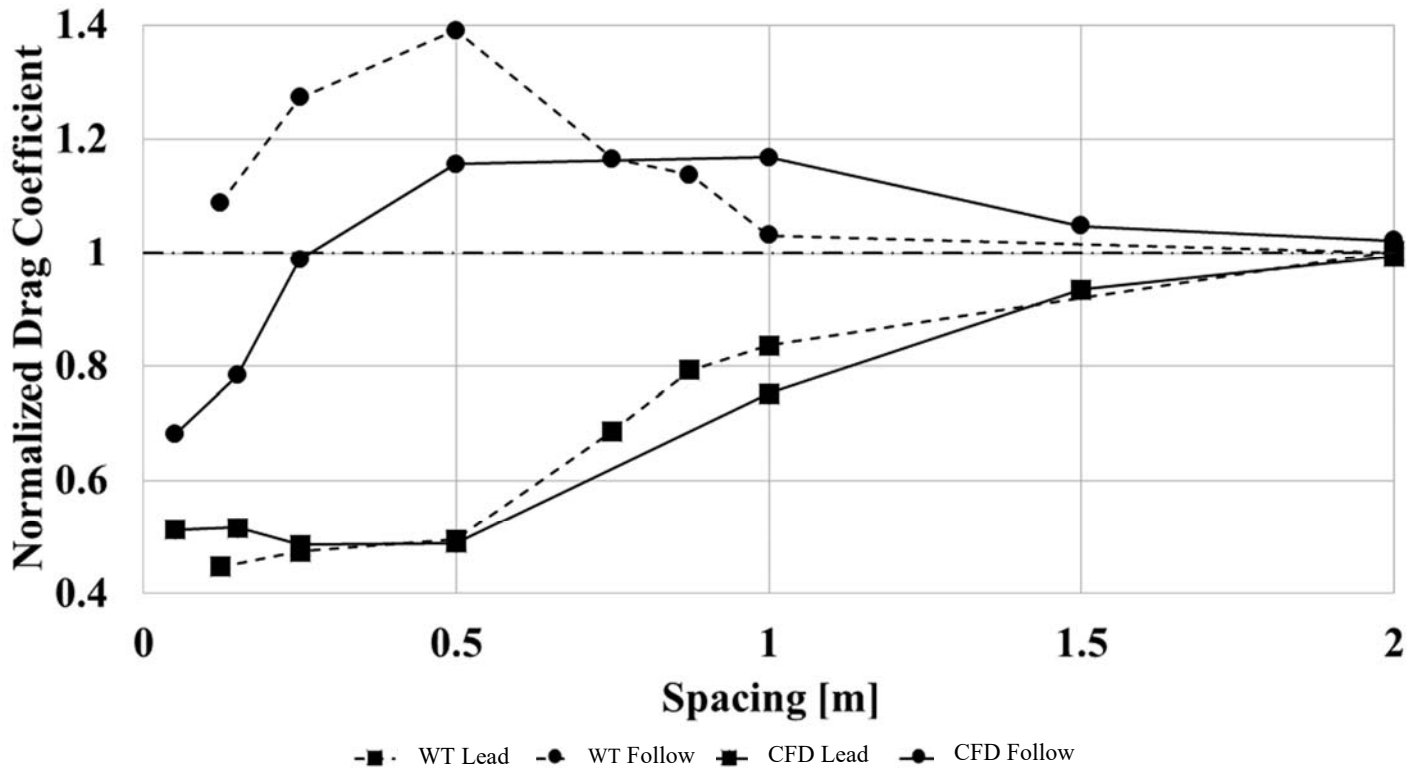
Figure 7: Normalized drag coefficient for two platooned Ahmed body vs. Se paration distance [15]

From a qualitative standpoint, the front body's predicted trend from the CFD results seems to match well nearly everywhere. Somewhat counterintuitively, the follower truck CFD results predict a local maximum at 50% of the body spacing. Despite the intuition, there seems to be some divergence in the close spacings, where the CFD simulations predict a significantly lower coefficient of drag than was realized in the wind tunnel testing. Watts hypothesized that the discrepancy in the follower truck was caused by the difference between the modeled zero-degree slanted Ahmed bodies, versus the wind tunnel results which were conducted using 15 degree slanted Ahmed bodies [15]. For the truck investigations, the non-slanted bodies were deemed more representative of the bluff geometry of the trailers, and thus as a validation were more useful in evaluating the effectiveness of various solution methods towards use in the truck simulations.

3.5 Single Truck Simulations

The final step prior to simulating platooned vehicles is to simulate that of a single truck to serve as a baseline for comparison for each set of simulations. As part of the FHWA project, two Peterbilt 579 tractors were leased for the duration of the contract, a photograph of which is shown in Figure 8.

Figure 8: Photograph of Auburn research Peterbilt 579 with Smartway style trailer attached

As part of the initial analysis, Watts simplified much of the geometry, removing many features which contributed very little to the overall solution [15]. Since the goal of the investigation is to characterize the drag reduction in terms of the separation distance, features that are relatively small compared to the overall length scale of the problem can be safely ignored. While this does not necessarily give fully accurate results in terms of predicting the absolute value of the drag coefficient for each of the vehicles, it is sufficient to show the relative trend of the drag coefficient with regards to separation distance of the platoon. Figure 9 shows a drawing of the Peterbilt 579 3D model generated in SolidWorks with some of the important dimensions of the vehicle labeled.

This model was used throughout the platooned vehicle simulations.
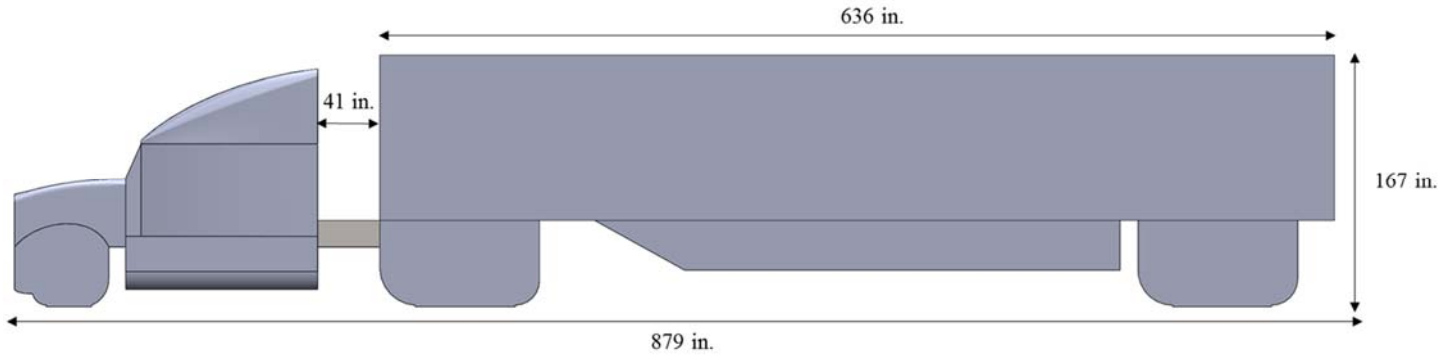
Figure 9: SolidWorks drawing of simplified Peterbilt 579 model

3.5.1 Single-Truck Surface Refinements

Conversion from a fully defined three-dimensional model to a discretized mesh degrades the fidelity of the solution model. Defining additional surface refinements helps provide additional elements and thus more resolution, particularly in areas of high curvature. The trucks represent a fairly complicated geometry, and thus several areas of additional surface refinements were generated to aid with the resolution in these specific areas. Figure 10 depicts an overall view of the surface refinements.
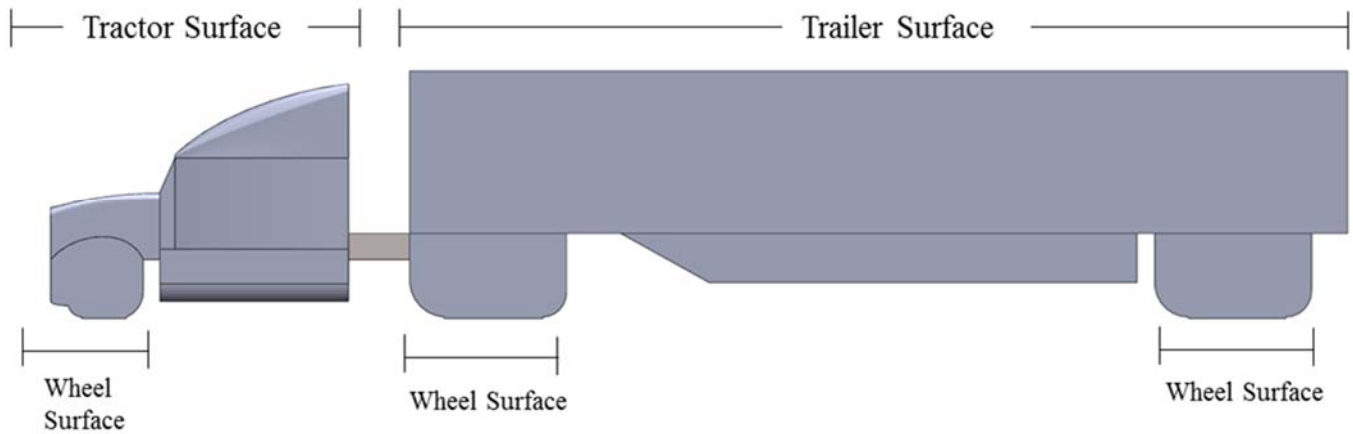
Figure 10: Overview of surface refinement regions

The wheel surface refinements are then further refined into an upper wheel and lower wheel, where the lower wheel is comprised of the region beginning with the curve and ending with the connection to the road. Table 3-6 describes the meshing parameters that are defined within each region shown in Figure 10.

Table 3-6: Surface refinement region parameters

Surface Refinement Region	Preferred Size
Tractor	10 inches
Trailer	15 inches
Wheel	10 inches
Lower Wheel	10 inches, 0.1 inch minimum size

3.5.2 Single-Truck Volume Refinements

Similar to the Ahmed body, a series of volumetric refinement regions were developed to enhance the resolution of the mesh in regions of high gradients. Figure 11 shows the 5 refinement regions for the single truck simulations.
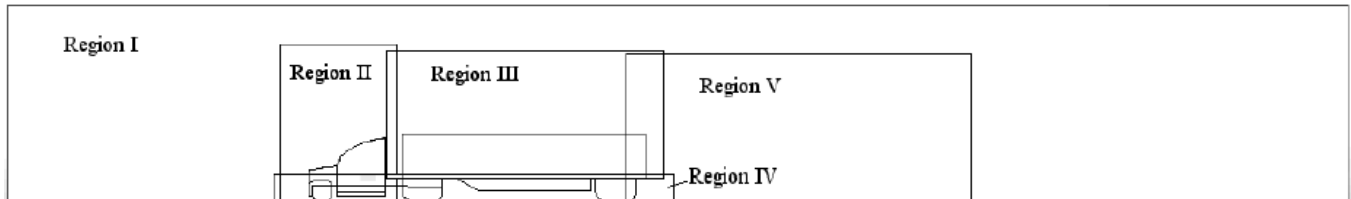
Figure 11: Overview of single truck refinement regions [15]

Region 1 represents the transition region to provide a smooth transition from the near-field to the far-field. Region II represents the cab of the vehicle, where there is a large gradient as the flow moves over the surface of the cab. Region III is the region over the trailer, where the wake is extending vertically. Region IV is the region representing the underbody of the vehicle, where complicated interactions between the vehicles and the road require sufficient resolution to be captured. Finally, Region V is the wake region, which requires sufficient gridding to capture the vortex structure within it to determine an accurate coefficient of drag. These five refinement regions, along with their corresponding dimensions and meshing characteristics are presented in Figures 12-16 and Table 3-7: Dimensions and meshing characteristics for refinement regions corresponding to Figures 12-16
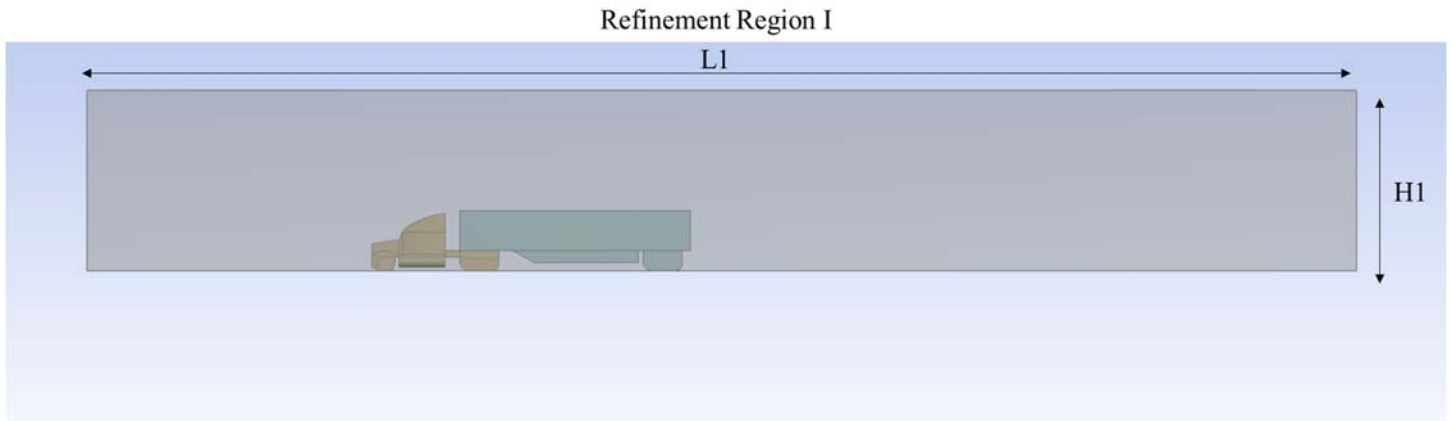
Figure 12: Refinement Region 1 with dimensions

.
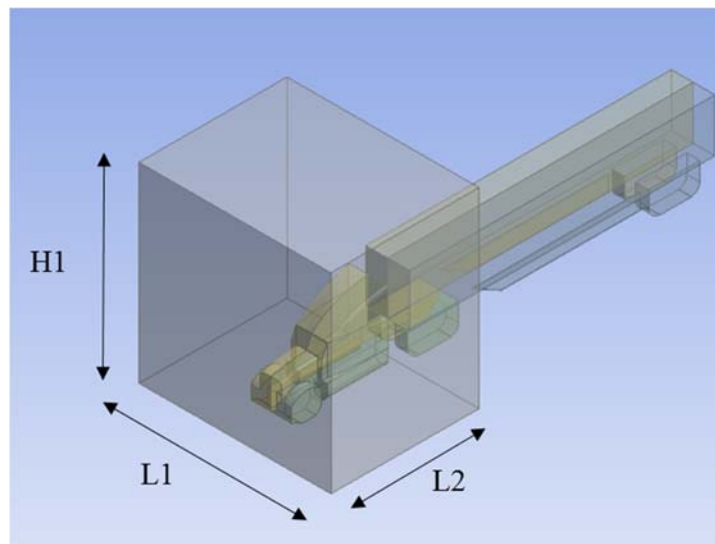
Figure 13: Refinement Region II with dimensions
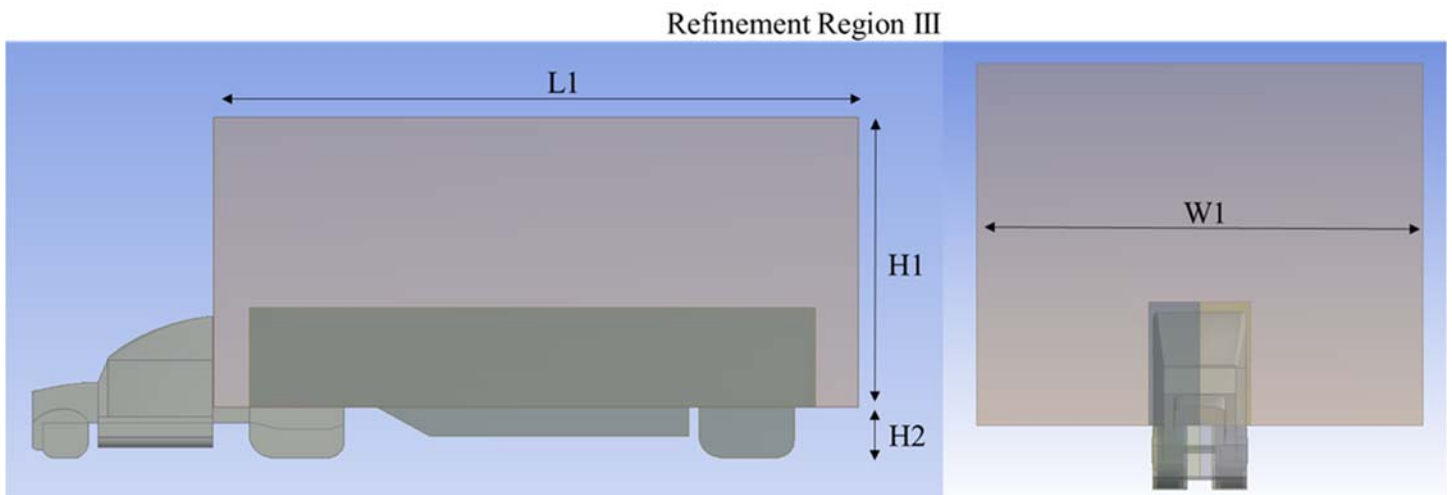
Figure 14: Refinement Region III with dimensions

Refinement Region IV
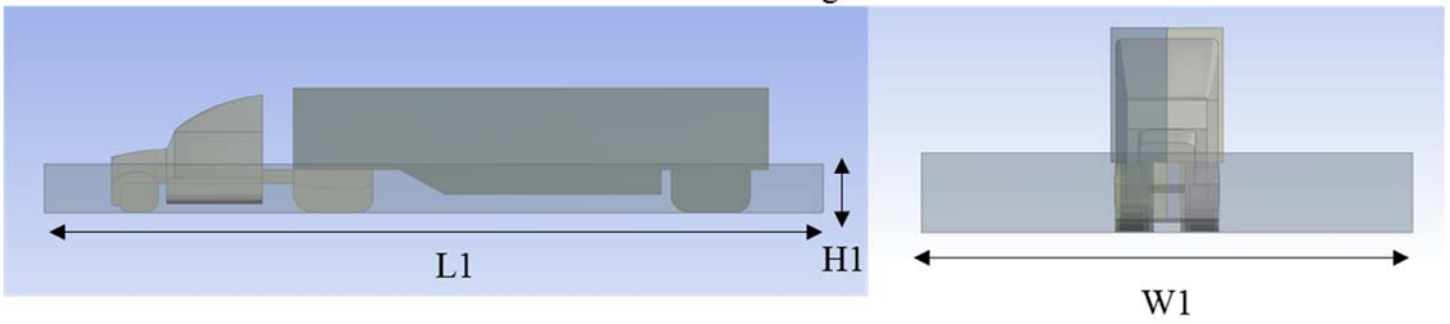
Figure 15: Refinement Region IV with dimensions

Refinement Region V
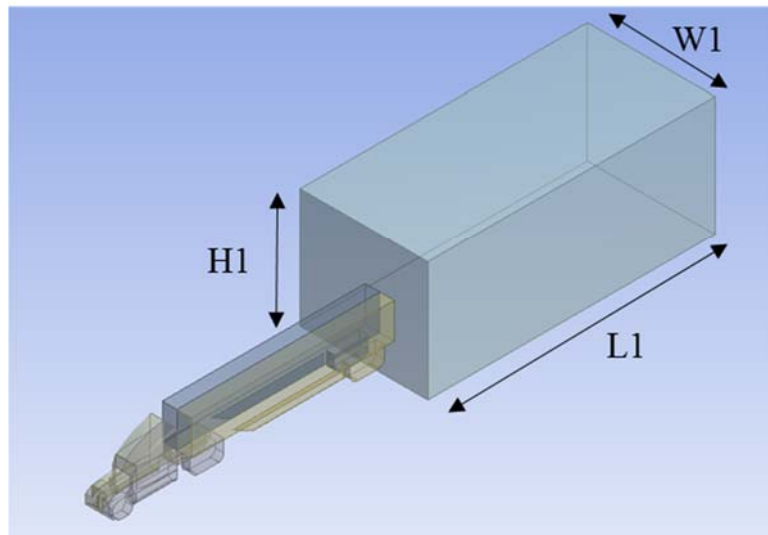
Figure 16: Refinement Region V with dimensions

Refinement Region I

Dimensions

H1 = 500 in.

L1 = 3500 in.

Width = 500in.

Meshing Characteristics

Element Size   0.9144 m

Local Min Size   0.0254 m

Growth Rate   Default

Refinement Region II

Dimensions

H1 = 400 in.

W1 = 400 in.

L2 = 300 in.

Meshing Characteristics

Element Size   0.9144 m

Local Min Size   0.0254 m

Growth Rate   Default

Refinement Region III

Dimensions

H1 = 325 in.

H2 = 57 in.

L1 = 725 in.

W1 = 400 in.

Meshing Characteristics	
Element Size	0.508 m
Local Min Size	0.0254 m
Growth Rate	Default

Refinement Region IV

Dimensions

H1 = 65 in.

L1 = 1042.4 in.

W1 = 400 in.

Meshing Characteristics

Element Size	0.3048 m
Local Min Size	0.0254 m
Growth Rate	Default

Refinement Region V

Dimensions

H1 = 375 in.

L1 = 900 in.

W1 = 400 in.

Meshing Characteristics

Element Size	0.508 m
Local Min Size	0.0254 m
Growth Rate	Default

These five regions of additional mesh refinements, coupled with a general volumetric sizing outlined in Table 3-8 fully define the volumetric meshing requirements for the single truck

simulation case. Wherever a value is not outlined in the Table 3-8, it was left as the default value generated by ANSYS.

Table 3-8: Global meshing parameters for single truck simulations

Sizing	
Advanced Sizing Function	Proximity and Curvature
Relevance Center	Fine
Smoothing	High
Transition	Slow
Min Size	0.0254 m
Max Face Size	3.0480 m
Max Size	3.0480 m
Minimum Edge Length	.010639 m
Inflation	
Automatic Inflation	Program Controlled
Inflation Options	First Aspect Ratio
First Aspect Ratio	5
Maximum Layers	5
Growth Rate	1.2
Growth Rate Type	Geometric
Maximum Angle	140°
Use Post Smoothing	Yes
Smoothing Iterations	10

This yielded a mesh size for the single truck consisting of 2653085 elements. This mesh database was then saved and imported into the FLUENT setup solution portion of the ANSYS workbench files.

3.5.3 Single-Truck Solution and Results

After the meshing database is saved, the final step before solution is to define the solution parameters and initialize the solution. To accomplish this, as discussed in Chapter 2, a pressure-based, coupled solution was utilized throughout all the simulations conducted. Table 3-9 shows the summary of all the parameters inputted into the FLUENT setup solution step. Any quantity not specified in Table 3-9 was left as the default value generated by FLUENT. Additionally, the domain was reordered using the Reverse Cuthill-McGee method to reduce the memory bandwidth required, and aid in the solution process.

Table 3-9: Summary of CFD solution parameters for single-truck simulations

Parameter	Value
Solution Methods	
Turbulence Model	Non-Transient RKE
Pressure-Velocity Coupling	Coupled
Pressure Solution Method	Standard
Momentum Solution Method	SOU
Turbulent Kinetic Energy	SOU
Turbulent Dissipation Rate	SOU
Initialization Method	Hybrid Initialization

Relaxation Factors	
Courant Number	50
Momentum Relaxation Factor	0.25
Pressure Relaxation Factor	0.25
Density Relaxation Factor	1
Body Forces Relaxation Factor	1
Turbulent Kinetic Energy Relaxation Factor	0.8
Turbulent Dissipation Rate Relaxation Factor	0.8
Turbulent Viscosity Relaxation Factor	0.8
Boundary Conditions	
Velocity Magnitude Inlet Condition	29.0576 m/s
Pressure Outlet Condition	0 Pa Gauge Pressure
Turbulence Model Parameters	
Type	Realizable k-ε
C2-Epsilon	1.9
TKE Prandtl Number	1
TDR Prandtl Number	1.2
Wall- Treatment	Non-Equilibrium Wall Treatment

3.6 Two-Truck Simulations

The next step in the analysis process was to simulate platooned vehicles. Having validated the

meshing and turbulence schemes using the Ahmed body, and then determining a coefficient of

drag for a single Peterbilt 579 model as a baseline, the vehicles were combined in a platooning configuration for simulation. Figure 17 depicts the bounding box comprising the control volume of air that was used in the two truck simulations.
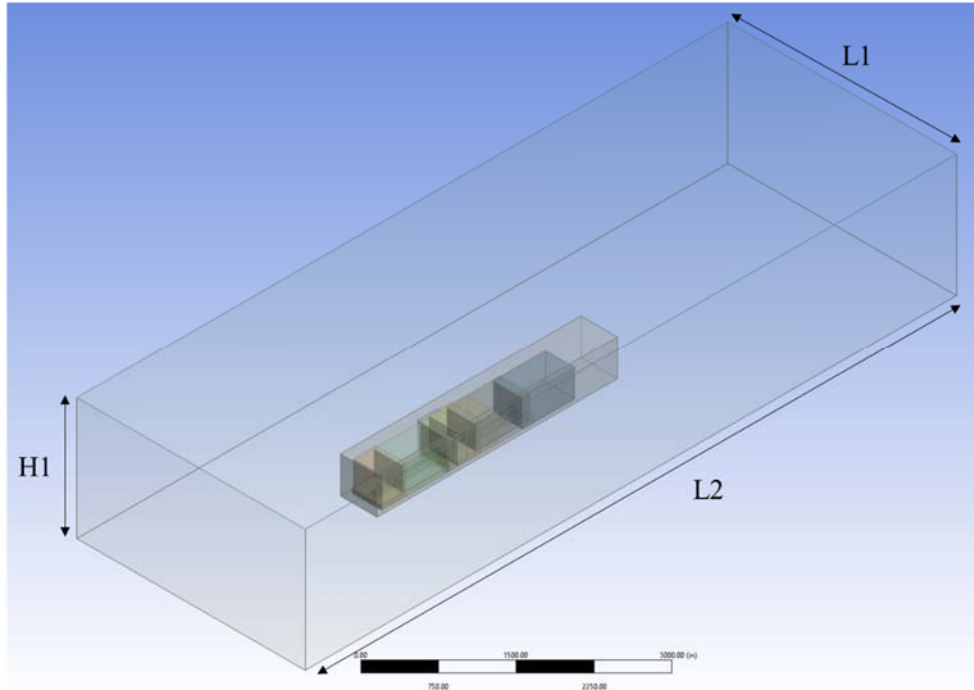
Figure 17: Depiction of Bounding box for Two-Truck Simulation

The dimensions shown in Figure 17 corresponding to Table 3-10 were held constant throughout the series of simulations.

Table 3-10: Dimensions of platooned vehicles bounding box

| H1 = 1500 inches |
| L1 = 3000 inches |
| L2 = 7000 inches. |

where H1 is the height of the bounding box, L1 is the width of the bounding box, and L2 is the length of the bounding box, comprised of two dimensions, 2500 inches from the front surface of

the bounding box to the front surface of the lead vehicle, and 4500 inches from the rear surface of the follower trailer to the rear surface of the bounding box.

3.6.1 Two-Truck Volume Refinement Changes

The confines of the above bounding box represent the control volume being meshed and solved for the platooning vehicle solution. Within this bounding box are a series of both volumetric and surface meshing refinements, which are similar to two sets of the original single truck volumetric and surface refinements. They differ in regards to volume refinement region I, where the distances are the same magnitude, but the rear surface of the volumetric refinement is defined from the rear surface of the follower trailer rather than the rear surface of the lead trailer. Figure 18 shows this new dynamic definition. In places where the refinement zones overlap due to insufficient separation distance, the lowest maximum size element is utilized.
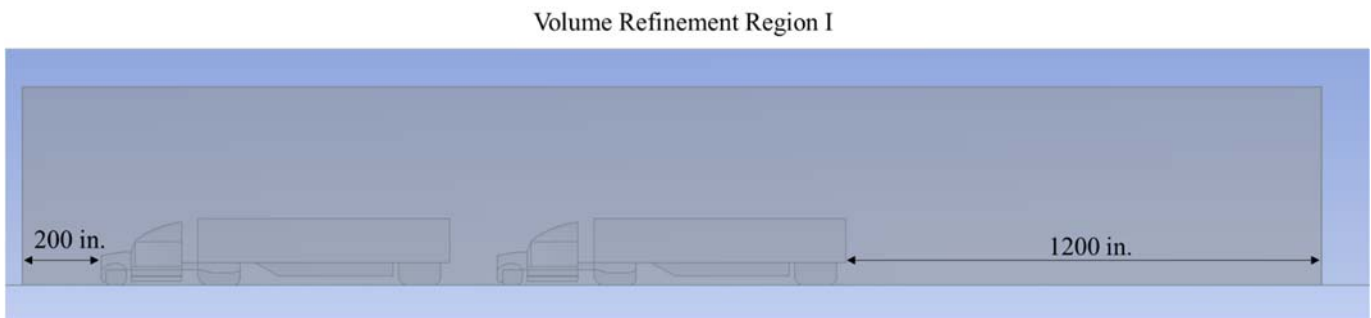
Figure 18: Volumetric refinement region 1 dynamic length definition for two truck platoons

The global meshing parameters remain the same as the single truck simulation, and the surface refinements simply consist of a second set identical set applied to the follower truck. Since the size of the bounding box increases with the separation distance, and more volume elements are required in between the vehicles, the total number of elements within the mesh varied with the separation distance. Table 3-11 summarizes the total number of volume elements in each mesh for each separation distance tested.

Table 3-11: Number of elements for each simulated separation distance

Separation Distance (ft.)	Number of Elements
10	4,684,539
20	4,742,006
30	4,748,209
40	4,792,167
50	4,821,888
60	4,864,276
70	4,894,380
80	4,909,448
90	4,941,851
100	4,958,136

3.6.2 Two-Truck Simulation and Results

In order to retain similarity between the Ahmed body validation case, the single truck baseline case, and the two-truck simulation case, the simulation solution parameters were not changed, which are summarized previously in Table 3-9.

After obtaining the coefficient of drag at convergence for each distance, the percent drag reduction was calculated through Equation (3.3).

$$\%\Delta C_{d,i} = \frac{C_{d,b} - C_{d,i}}{C_{d,b}} \tag{3.3}$$

where $\%\Delta C_{d,i}$ is the percent drag reduction for either the front or rear truck, $C_{d,b}$ is the coefficient of drag for the single truck baseline simulation, and $C_{d,i}$ is the coefficient of drag for either the

lead or follower truck for each separation distance. Figure 19 shows the results of the initial two-truck simulation series for the percent drag reduction versus separation distance.
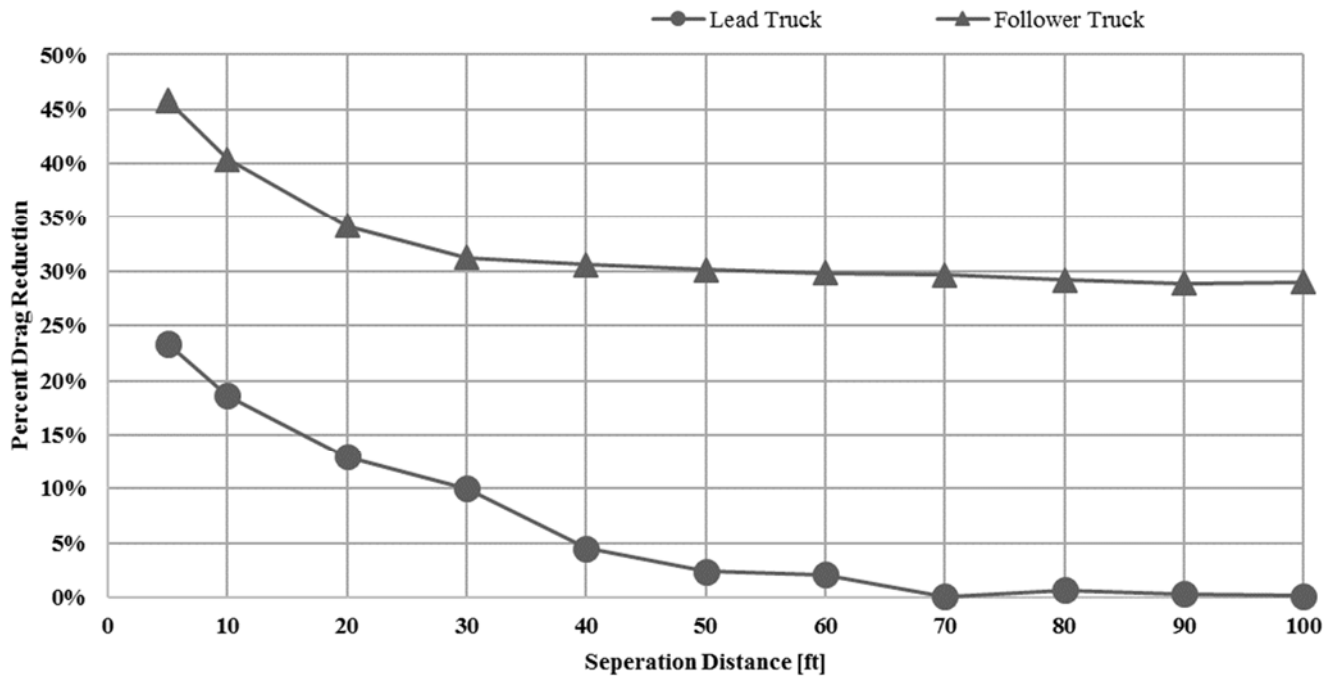
Figure 19: Percent drag reduction vs. separation distance simulation results for two truck platoon

From this trend, it is evident that as the separation distance diminishes, the percent drag reduction increases, in a monotonic fashion. This then entails that the optimum separation distance for achieving maximum percent drag reduction, both for each vehicle as well as the combined platoon, occurs at the minimum safe operating separation distance. The results from this initial survey appear to qualitatively match the previous general consensus. Results from Energy ITS's fuel economy testing, as well as from the California PATH program's wind tunnel results are shown in Figure 20 [25,26].
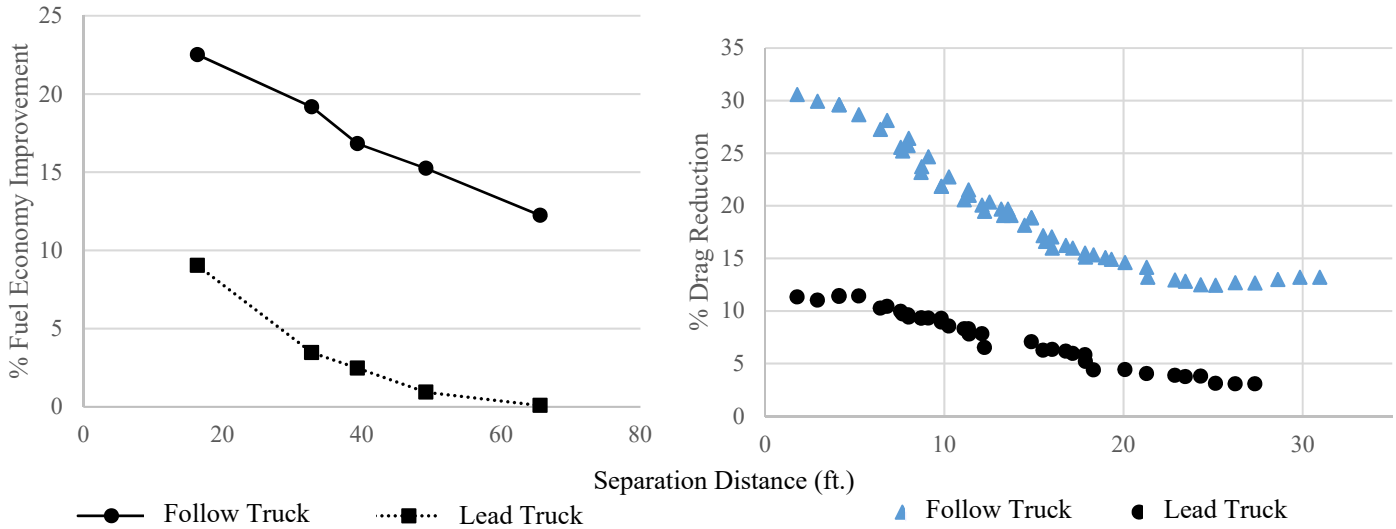
Figure 20: Energy ITS fuel economy measurements (left) [25] *and California Path Project wind tunnel measurements (right)* [26]

Both trends in Figure 20 show that as the separation distance diminishes the drag reduction, or fuel economy improvement, increase. As noted previously, the Energy ITS results should be heavily qualified in that they represent both a different type of vehicle geometry, with a more European style tractor, characterized by a flatter front surface resulting in a more rapid transition to the trailer, as well as utilizing unloaded trailers. Unloaded trailers drastically reduce the operating weight of the vehicles, and since the total drag on the vehicles is the combination of the rolling resistance and the aerodynamic drag, a lower weight entails that a larger portion of the total drag is caused by the aerodynamic drag. In a desire to further validate these results, a fuel economy test was then conducted by Auburn University to provide data for validation, which is described in Chapter 4.

Chapter 4

SAE Type II Fuel Economy Test Results

In order to validate the two truck testing performed by Andrew Watts, the two Auburn test vehicles were taken to the 7.5 mile test track at a large test track facility in Ohio, shown in Figure 21 to conduct an SAE Type II Fuel Economy test, according to the 1986 standard [38]. While there exists an updated 2012 standard, the 1986 standard was chosen due to several factors. The more stringent mileage requirements in the 2012 standard were impractical to achieve given the relatively short testing window. This, coupled with the recommendation of the Technology and Maintenance Council (TMC) of the ATA, led to the usage of the 1986 standard rather than the more recent 2012 standard.

Figure 21: Image of large test facility, showing 7.5-mile test track

4.1 SAE Type II Fuel Economy Test Setup

The SAE Type II standard requires a rigorous inspection of the vehicles to ensure consistency between the vehicles. In addition, the test requires a control vehicle, which is used to normalize the results of the fuel economy testing. By dividing the fuel consumption by the control truck, the achieved effect is to help eliminate external variables from the analysis. Since the control truck is affected by the same weather conditions as that of the platooning vehicles, it helps to ensure a consistent, accurate measurement of the fuel economy gains provided by the platooning system.

In addition, the J1321 standard was developed with the intention to test a single trucks' fuel economy. Therefore, some modifications to the standard were implemented to accommodate the two-truck platoon. The primary modification was the addition of an electronically controlled switch which allowed for switching to the auxiliary test fuel tank. This was required so that the test period would consist only of when the two trucks had established platooning, so that variances in the time required to initialize the platoon were not represented in the data. Adding the same switch to the control truck was not necessary, due to being able to have the control truck "on-test" throughout the duration of the run. The control truck then completed seven complete laps "on-test" including the ramp on and off. Since this time was consistent throughout the runs, and both trucks were normalized by the same control, this was deemed satisfactory for the test.

Since there were only two test vehicles provided to Auburn University, a third test truck was acquired for the duration of the testing in Ohio to serve as the control vehicle. To mitigate as many external factors as possible, the control tractor should be similar to the two test vehicles used in the platoon. To accomplish this goal, a 2013 Peterbilt 579 was selected as the control tractor for the duration of the Ohio fuel economy testing. Once again, to minimize the differences between the control trucks and the platooning vehicles, the standard 53 foot trailers utilized for the duration

of the testing sequence were kept constant, and utilized the same features and weight, legally labeled 65,000 lbs. Table 4-1 summarizes the relevant features of each vehicle for comparison of the trucks used for testing.

Table 4-1: Features of each vehicle for SAE Type II Fuel Economy test

Specification	Lead Tractor-Trailer	Follower Tractor-Trailer	Control Tractor-Trailer
Manufacturer	Peterbilt	Peterbilt	Peterbilt
Model	579	579	579
Model Year	2014	2014	2013
Vehicle Mileage at Test End	6,595.9 mi	6,524.7 mi	16,173 mi
Engine Manufacturer	Paccar	Cummins	Cummins
Engine Model	MX-13	ISX15 415 ST2	ISX15 415 ST2
Engine Model Year	2014	2014	2013
Emissions Equipment	DDI, TC, CAC, ECM, EGR-C, OC, SCR-U, PTOX	EGR, PTOX, SCR	EGR, PTOX, SCR
Transmission	Eaton Fuller Automated 10-speed	Eaton Fuller Automated 10-speed	Eaton Fuller Automated 10-speed
Retarder/ Regenerative Braking	Engine Brake	Engine Brake	Engine Brake
Tires (Front Axle)	Michelin X Green XZA3	Michelin X Green XZA3	Bridgestone Eco Pia R283

Tires (Driven Axles)	Michelin Energy XDA	Michelin Energy XDA	Bridgestone Eco Pia M710
Trailer Configuration	53 ft Van Trailer with angled side skirts	53 ft Van Trailer with angled side skirts	53 ft Van Trailer with angled side skirts
Trailer Manufacturer	Wabash	Wabash	Wabash
Trailer Model	TRA VAN DVCVHPC	TRA VAN DVCVHPC	TRA VAN DVCVHPC
Trailer Height	13' 6"	13' 6"	13' 6"
Trailer Width	102"	102"	102"
King Pin Set Back	36"	36"	36"
Trailer Axle Longitudinal Position	40'	40'	38'
Trailer Side Skirt	DuraPlate AeroSkirt	DuraPlate AeroSkirt	DuraPlate AeroSkirt
Tires (Trailer Axles)	Goodyear Fuel Max Tech G316 LHT	Goodyear Fuel Max Tech G316 LHT	Goodyear Fuel Max Tech G316
Distance from Rear of Trailer Side Skirt to Front of Trailer	36"	36"	10-12"

Once brought to the facility, the vehicles were inspected to ensure that the tires were at the correct operating pressures, and that there were no engine malfunctions which required attention. After resolving any issues that were encountered, the trucks were driven around the test track for 45 minutes to warm up both the engine and the tires. Once warmed up, the electronic switch was activated at the 4.8-mile marker on the track, using radio communications to synchronize the

switch between the two platooning vehicles. The trucks were then considered "on-test", and completed 6 laps while platooning at 65 mph, where the switch was activated once again, returning the vehicles to their primary fuel tanks. The trucks were then driven to the pit-stop location, where the auxiliary fuel tank was removed and the gravimetric fuel consumption was measured. This was then repeated three times, where the given repeatability fell within a 2% bound as specified by J1321. These three repetitions then represented one successful run at each test criteria. For this test, the separation distance was the primary variable of interest, and thus all other parameters were kept constant. To validate the CFD results, the following separation distances were tested: 30ft, 40ft, 50ft, 75ft, and 150ft. Additionally, each truck was run separately, using the standard J1321 standard to determine that individual truck's baseline fuel consumption. This allows for calculation of fuel savings, rather than fuel consumption reduction, which is a slightly more conservative estimate.

4.2 Fuel Consumption Calculations and Results

J1321 details a gravimetric method for determining the amount of fuel consumed by the vehicles during testing [38]. First, the weight of the fuel consumed is determined by directly subtracting the weight at the end of the test from the initial weight measured before the test had begun. This is then normalized by dividing by the control truck's fuel consumption weight. This is then differenced with the baseline's normalized value, then divided by the baseline value to provide the percent fuel savings achieved by each vehicle:

$$L_{FS} = \frac{T_L/C - B_L/B_C}{B_L/B_C} \tag{3.4}$$

$$R_{FS} = \frac{T_R/C - B_R/B_C}{B_R/B_C} \tag{3.5}$$

Where L_{FS}, R_{FS}, are the lead and follower truck's fuel savings, respectively, T_L is the test truck's test consumed fuel weight, B_L is the lead truck's baseline consumed fuel weight, B_C is the control truck's baseline consumed fuel weight, and C is the control truck's test consumed fuel weight. This value is used as the percent fuel savings for each run and is averaged over the three runs to achieve the average percent fuel savings for a separation distance, for both the lead and front truck. The results for the entire series of testing are presented in Figure 22, and are compared to the CFD simulation results shown in Figure 19.
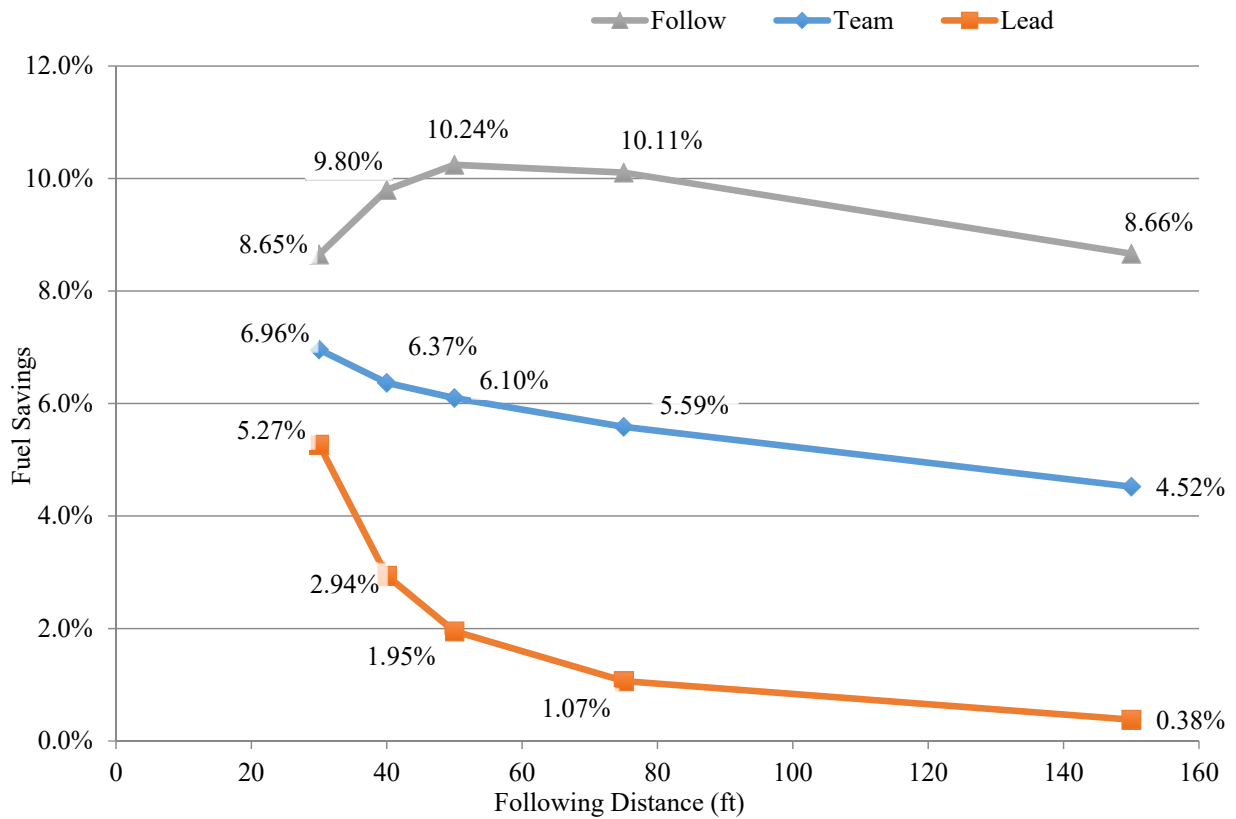

Figure 22: Percent fuel savings results from Ohio Type II Fuel Economy Test

4.3 Analysis of Fuel Economy Results

Inspection of the fuel economy results shows that both the overall platoon's fuel savings' and the front truck's fuel savings monotonically increase as the separation distance diminished. This is similar to the prediction of the two-truck simulations. Despite good agreement with the overall platooning trend and the front truck, however, the follower truck displays a contradictory trend. As shown in Figure 22, the follower truck has a local maximum at 50 ft, and then declines as the separation distance diminishes. Several potential reasons are presented in the following sections as a means to explain this contradictory trend, including an unfavorable temperature rise caused by low convective heat transfer across the engine block, controller dithering, and lateral offset as an additional aerodynamic effect. In an attempt to eliminate as many potential explanations as possible, several of these factors were investigated.

4.3.1 Thermodynamic Losses

During the National Renewable Energy Laboratory's (NREL) testing in Texas, the follower truck exhibited a similar trend to the one observed during Auburn's testing in Ohio for several of their test runs, as shown in Figure 23 [27]. In their analysis of these runs, NREL made note that the engine fan experienced a significant duty cycle in some of the runs with small separation distances [27]. This potentially implied that the engine temperature was rising, most likely due to lower convective heat transfer across the front surface of the follower truck. This is consistent with the original predictions of the CFD analysis, since the primary mechanism of drag reduction on the follower truck is a reduction in the velocity experienced by the front surfaces of the follower truck.
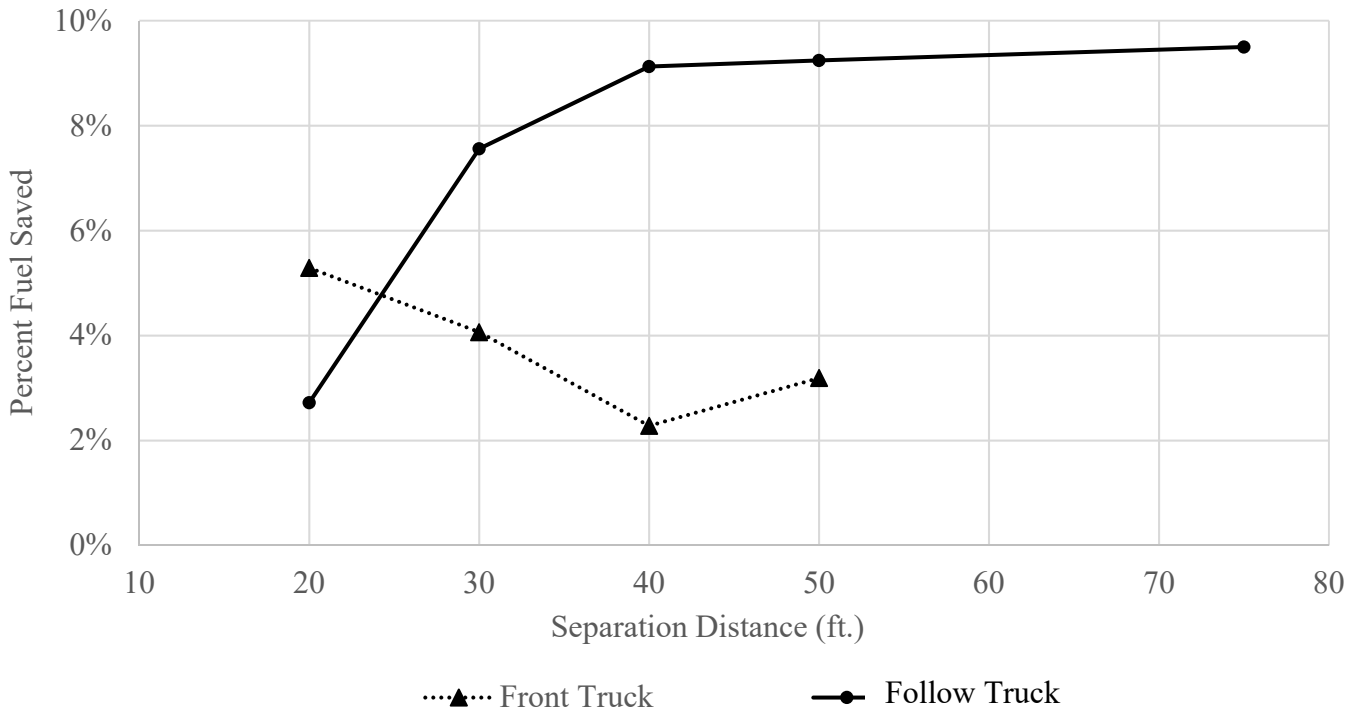
Figure 23: Selected run from NREL Uvalde Test Campaign, 65 mph, 65K lbs loaded weight [27]

In general, the convective heat transfer can be calculated via Newton's Law of Cooling in the following form:

$$q_{conv} = h\left(T_s - T_\infty\right) \tag{3.6}$$

where q_{conv} is the specific convective heat transfer, h is the convective heat transfer coefficient, T_s is the temperature of the convective surface, and T_∞ is the temperature of the free-stream flow.

While this equation does not depend on the velocity, the convective heat transfer coefficient is a strong function of the fluid's properties, including the Reynolds number. The coefficient of convective heat transfer can then be written as:

$$h = \frac{0.664k \, \mathrm{Re}_x \, \mathrm{Pr}^{0.33}}{x} \tag{3.7}$$

where k is the thermal conductivity, Re_x is the Reynolds number, Pr is the Prandtl Number, and x is the reference dimension. From this equation, it is evident that the coefficient of convective heat transfer is strongly dependent on the Reynolds number, which is in turn strongly dependent on the velocity through the relation:

$$\text{Re}_x = \frac{\rho V x}{\mu} \tag{3.8}$$

where Re_x is the reference Reynolds number, ρ is the density of the fluid, V is the velocity of the fluid, x is the same reference dimension as in Equation (3.7), and μ is the dynamic viscosity.

From these three relationships, it is clear that as the velocity of the fluid increases, so too does the convective heat transfer. Figure 24 shows the velocity magnitude of the air surrounding the follower truck's engine block, as predicted by the CFD analysis. As previously stated, the primary mechanism for drag reduction acting on the follower truck is the effectively reduced velocity of air behind the lead truck, accomplished through slipstreaming the follower truck.
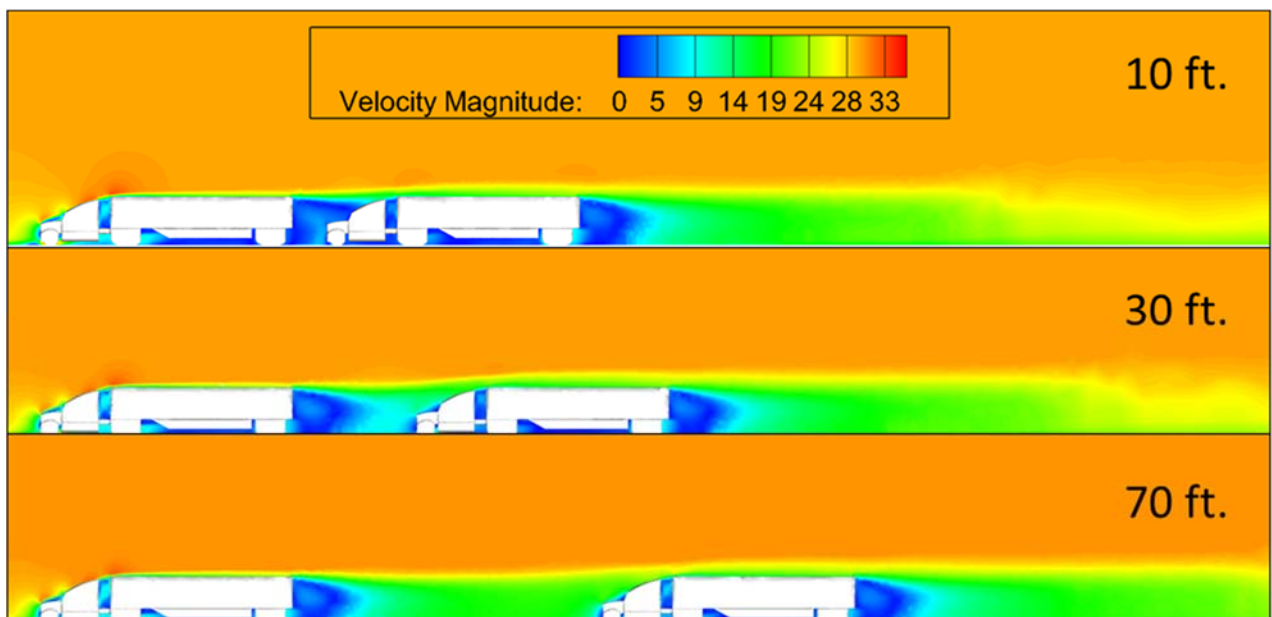
Figure 24: Two truck velocity magnitude for various separation distances [15]

58

During NREL's testing, this potential for lower convective heat transfer may have been exacerbated by the high temperatures during the testing, reaching up to nearly 90 degrees Fahrenheit [27]. Unlike NREL's testing however, the fuel economy test in Ohio occurred with relatively low nominal temperatures of approximately 70 degrees, and there was no engine fan duty cycle through any of the testing.

In addition to the engine fan duty cycle, several temperature parameters were recorded for the test runs. Figure 25, shows the relative ambient temperatures, measured on the front of the engine block using the engine's temperature probe outputted via the CAN bus, for both the lead and follower trucks. Once again, to eliminate external factors such as the local overall ambient temperature of the surroundings, the values are normalized by the control truck.
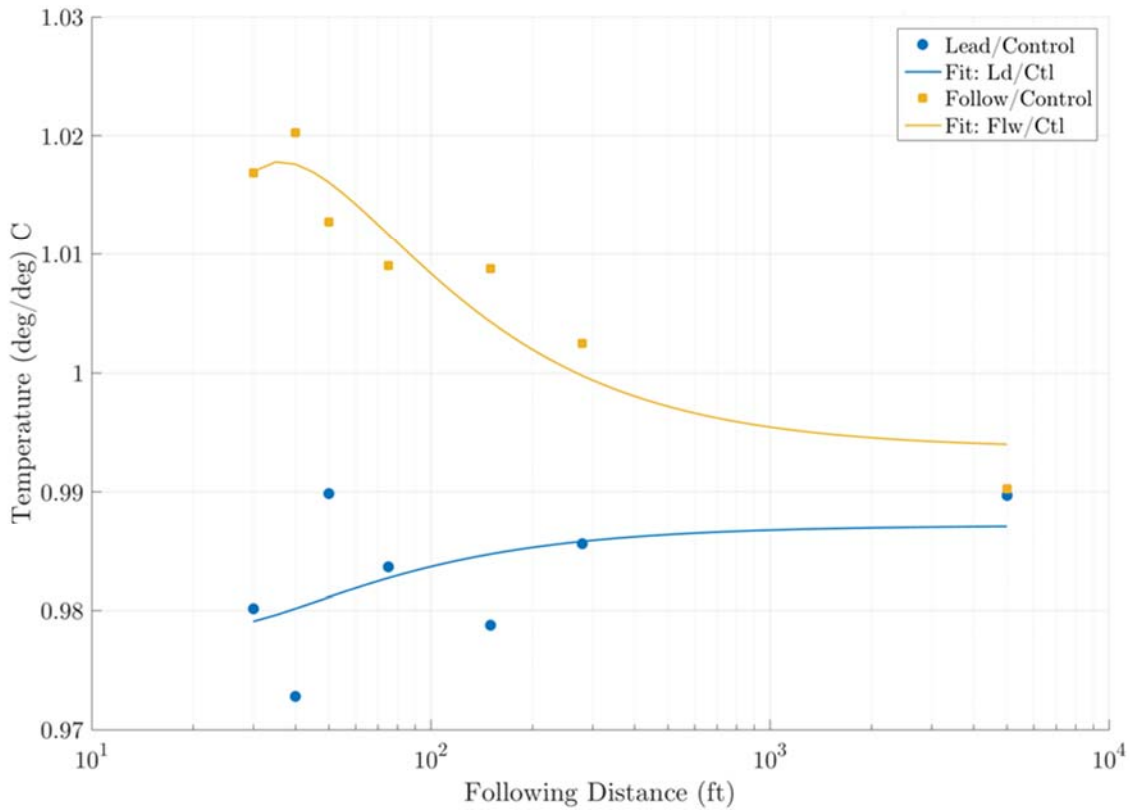
Figure 25: Mean ambient temperature of lead and follower trucks normalized by control truck mean ambient temperature [39]

As seen in Figure 25, as the separation distance diminishes, there appears to be a trend where the ambient temperature recorded for the follower truck rises. However, the rise in normalized temperature is comparatively very small. This is most likely caused by various forms of heat generation from the front vehicle, including tire friction and engine exhaust.

In addition to the ambient temperature, the engine coolant temperature was also recorded during all the fuel economy tests. The mean engine coolant temperature for each separation distance tested is presented in Figure 26. From the data presented in Figure 26, there does not seem to be a strong correlation between the engine coolant temperature and the percent fuel savings achieved for each truck, but rather, it is strongly correlated to external factors, which are exhibited by the control truck.
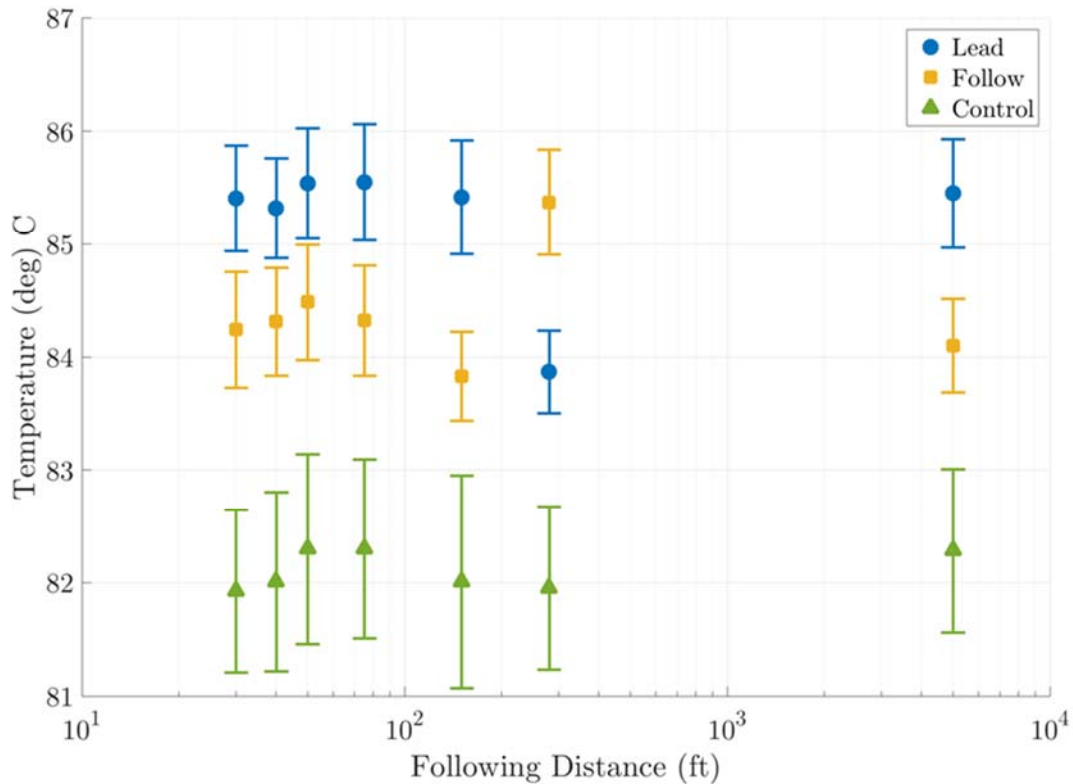
Figure 26: Mean engine coolant temperature vs. separation distance for Auburn Ohio fuel economy test [39]

From the data presented in Figure 26, there does not seem to be a strong correlation between the engine coolant temperature and the percent fuel savings achieved for each truck, nor for the local ambient temperature. Additionally, while the lead truck nearly always experienced higher coolant temperatures, this may be due to the higher amount of fuel burned during testing, or simply due to the engine differences between the two trucks. The engines between the two tested trucks as noted previously are significantly different, and thus may have different operational temperatures.

Without a more involved study, it is impossible to eliminate the possibility that engine temperature is not playing a role in the degradation of the follower truck's fuel savings while in platoon, but the current analysis seems to suggest that there is another effect which is significantly contributing to the higher-than-predicted fuel consumption of the follower truck at close following distances.

4.3.2 Controller Dither

Another potential explanation for the higher fuel consumption at close spacings was a phenomenon called controller "dithering." During prior testing of a previous iteration of the Peloton prototype, it was discovered that as the following distance diminished, the controlling algorithm became more aggressive with the control of the separation distance. In the previous testing, it was determined that as the frequency of changes between the torque request rate increased, so too did fuel emissions, despite the engine speed remaining relatively constant. This led to the conclusion that the torque dither (rapid changes in the percent torque requested) caused an increase in the amount of emissions produced by the engine.

The testing conducted in Ohio utilized a new version of the prototype Peloton DATP system, for which the torque dithering was significantly reduced. In general, if the engine is resisting a

physical force, such as increased aerodynamic drag, the mean torque delivered by the engine should increase as the separation distance decreases beneath 50 ft. This would indicate that there is some resistance which the engine must overcome. Figure 27 shows the mean torque after the curves from the test track and other large-scale periodic oscillations have been filtered from the data.
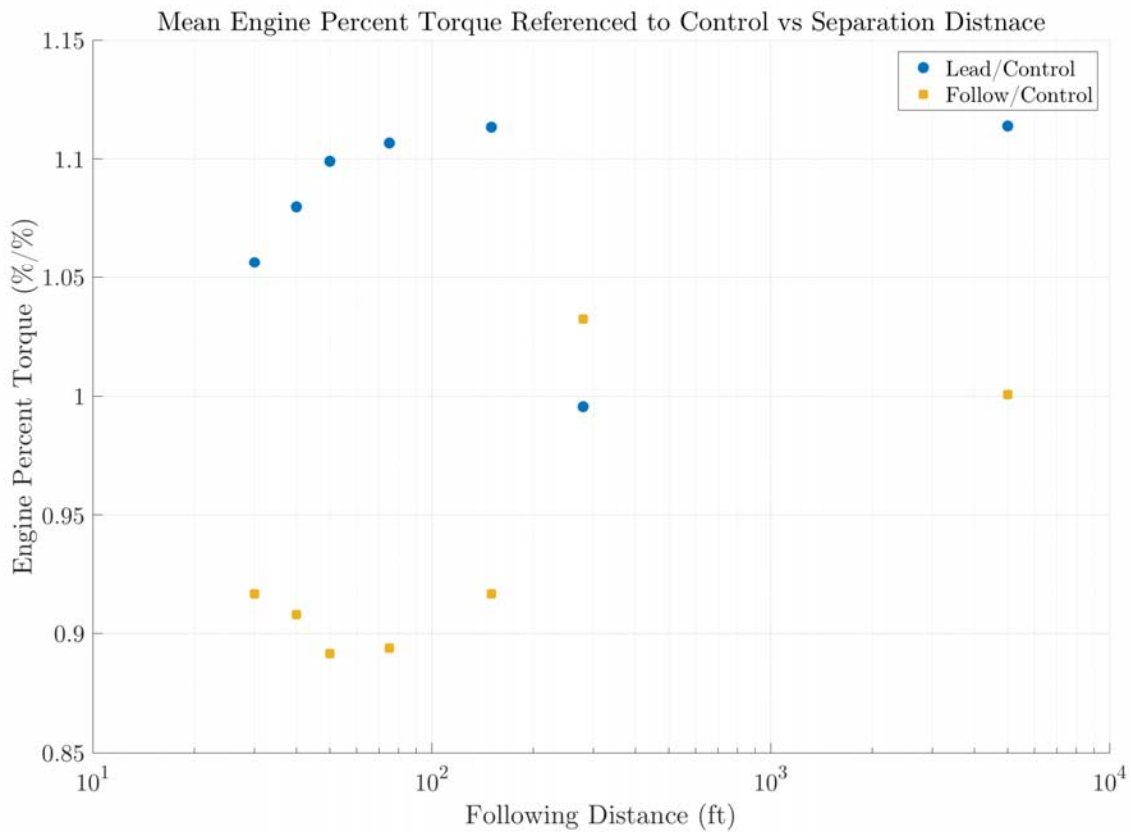
Figure 27: Mean engine percent torque normalized by control truck [39]

From Figure 27, it is evident that there is the expected increase in engine torque delivered, signifying that there is most likely a resistance that is being overcome at close distances for the follower truck. In previous testing, however, it was discovered that the frequency of change in the percent engine torque demanded had a significant impact on the emissions of the engine, as well as the drag experienced by vehicles in the platoon [39],[40]. This in turn is most likely due to a

change in the way the engine is consuming fuel. Therefore, the mean average is not sufficient to determine the characteristics of the torque dither.

The next metric used to characterize the controller behavior was the standard deviation of the engine torque delivered. The standard deviation characterizes how often and how much the data set strays from the mean, and thus is a good metric for how frequently the engine percent torque is changing. Therefore, if the controller is a strong factor in the degradation of the fuel consumption for the follower truck, the standard deviation of the engine torque delivered should rise as the separation distance diminishes. Figure 28 shows the filtered engine percent torque delivered throughout the Ohio testing.
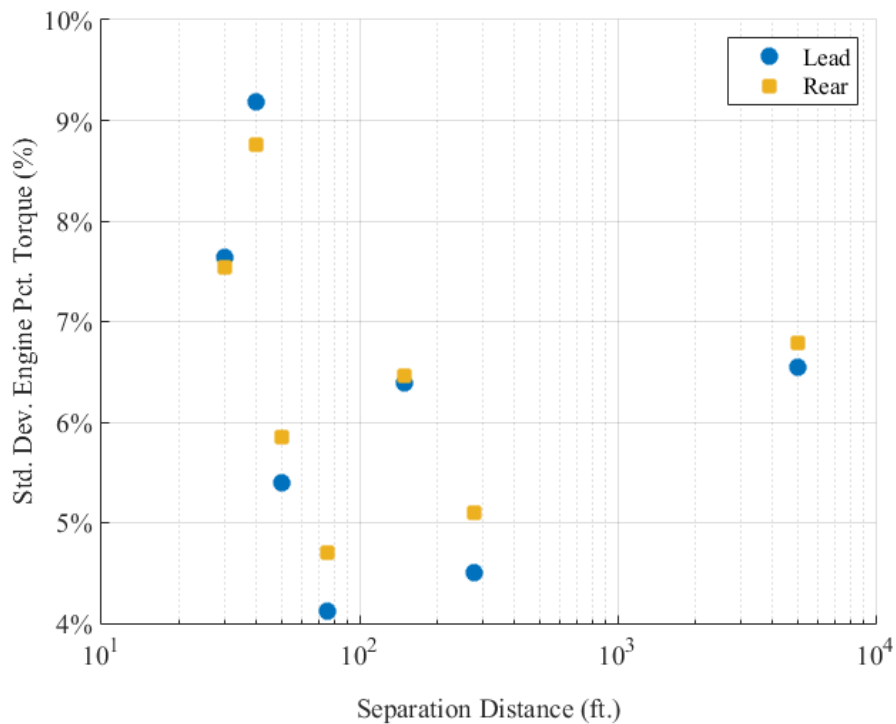

Figure 28: Standard Deviation in the Engine Percent Torque vs. Separation Distance [39]

Once again, there appears to be little correlation between the standard deviation of the normalized engine percent torque and the separation distance. With a strong correlation between the mean engine torque, and low correlation between the standard deviation, one final parameter

to check is to ensure that the frequency of the delivered torque doesn't increase as the separation diminishes. Figure 29 shows the Fourier transform of the delivered torque. The data was recorded at 5 Hz, and thus the resolved frequency is only 2.5 Hz. There is a large secondary spike at a nominal 0.0024 Hz, which corresponds to a period of almost 7 minutes. This secondary spike is most likely due to the small incline and decline present in each straightaway of the track. Past this secondary peak, there is no content higher in the spectral range, which is not shown for readability in Figure 29. Since the sampling frequency is comparatively low to that of the commanding frequency, it is still not determinate that the frequency of the percent engine torque being requested is not separation distance dependent, but there appears to be no dependence in the range of 0-2.5 Hz.
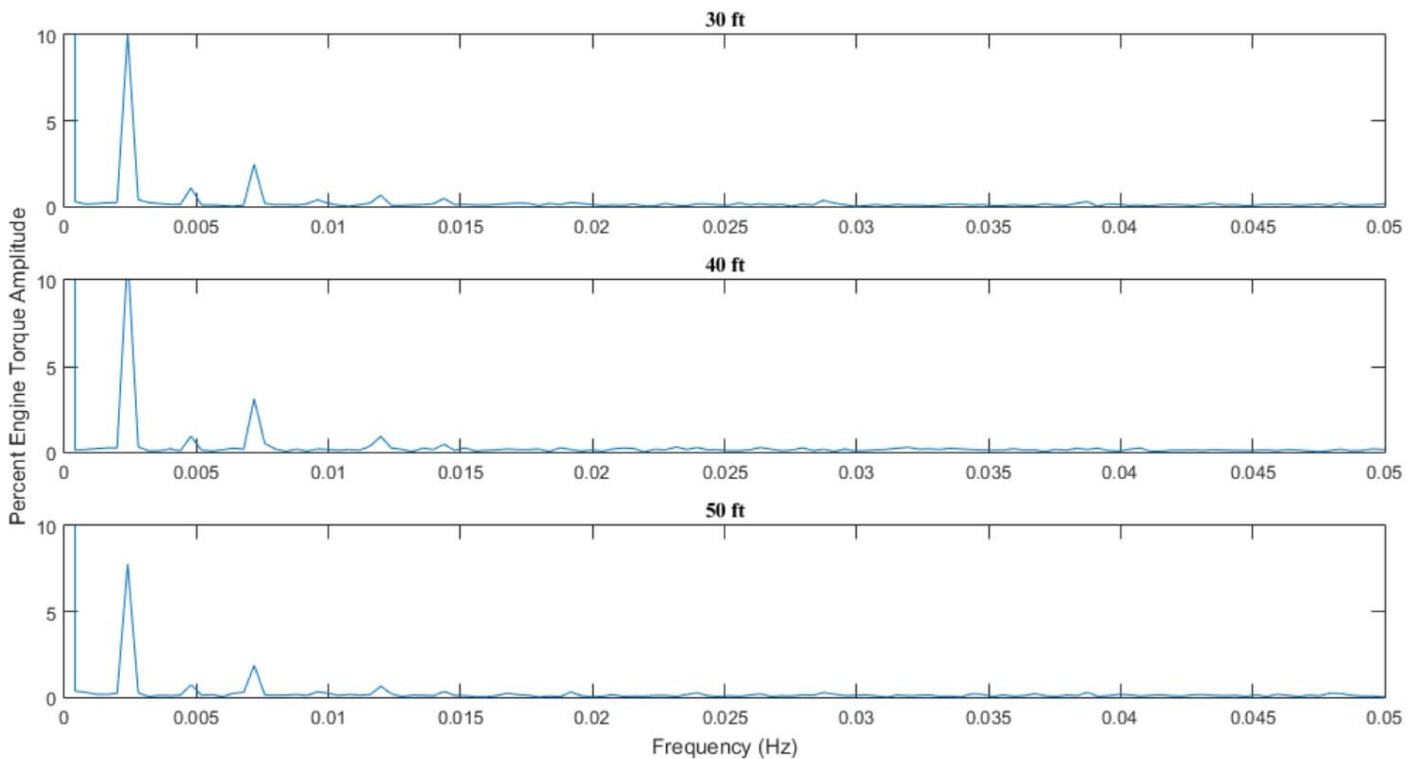

Figure 29: Fourier transform of engine torque delivered for various separation distances

These analyses provided some confidence that the controller's torque behavior is not playing a significant role in the degradation of the follower truck's fuel economy trend, at least in terms of

the throttle control. Additionally, the strong correlation between the mean delivered torque and the fuel economy results signifies that there is most likely a force which the follower truck is having to overcome which is contributing to the lower than predicted fuel savings experienced during the Ohio testing.

4.3.3 Other Contributing Factors

The previous sections outlined several possible explanations for the follower truck's trend which was contradictory to the original two truck simulations' predictions of monotonic fuel economy decrease at closer separation distances, while being similar at far separation distances. While not meant to be an exhaustive list of all possible explanations, these were several explanations that seemed highly likely. The previous sections also presented some logic explaining why they are potentially unlikely to be the primary contributing factor to the degraded follower trend. One additional theory proposed is that the follower truck is laterally offset during the testing, since the steering is being controlled by a driver rather than the system. This is due to observations during testing that the follower truck experienced some buffeting from the front truck.

Unfortunately, an accurate lateral offset determination was not able to be determined from the test runs previously conducted. However, since there is an academic interest in understanding how a lateral offset may impact a platooning system an additional CFD analysis was conducted to determine the effect of lateral offset on aerodynamic drag reduction, since the addition of lateral control represents a significant design choice when designing and implementing a platooning system. Therefore, the next chapter outlines the investigation into the potential negative impacts of lateral offset in more depth than the previous analysis.

Chapter 5

Analysis of Lateral Offset on Drag Reduction

The following section explores one of the possible explanations for the follower truck's degraded fuel performance at closer following distances. As noted previously, some buffeting was observed during the testing which led to the hypothesis that the trucks were potentially experiencing meaningful lateral offset during operation. Due to the mechanics of platooning, lateral offset has the potential to degrade the aerodynamic performance, and thus fuel economy performance, of the vehicles since the follower truck will no longer be shielded from the free-stream flow at close spacings and experience a higher-pressure distribution on its front surface.

5.1 Methodology

In an attempt to remain as consistent as possible, the lateral offset cases were simulated using the same basic parameters as the centered 2-truck cases. Simulations were conducted for each of the same separation distances at lateral offsets of 1ft. and 2ft. Two feet was chosen as a practical operating maximum, where both trucks are on opposite sides of the same lane.

Simulating lateral offsets presents slight differences to the simulation methodology. One of the largest difference in the initial setup of the offset platoons, is that the mesh refinement regions were widened to accommodate the lateral offset. Rather than just shifting the refinement box to the new center point of the offset vehicle, the refinement boxes were extended with twice the lateral offset, since the Region of Interest (ROI) around the vehicles is also extended when the vehicles are simulated with a lateral offset. Figure 30 shows the new control volume refinement regions, which are similar to that of the regular two truck platoon, shown previously in Figure 11. The overall length of these refinement volumes is defined dynamically based on the separation distance

of the platooned trucks, however the ends are always a fixed distance away from surfaces of the vehicles, as shown in Figure 30.
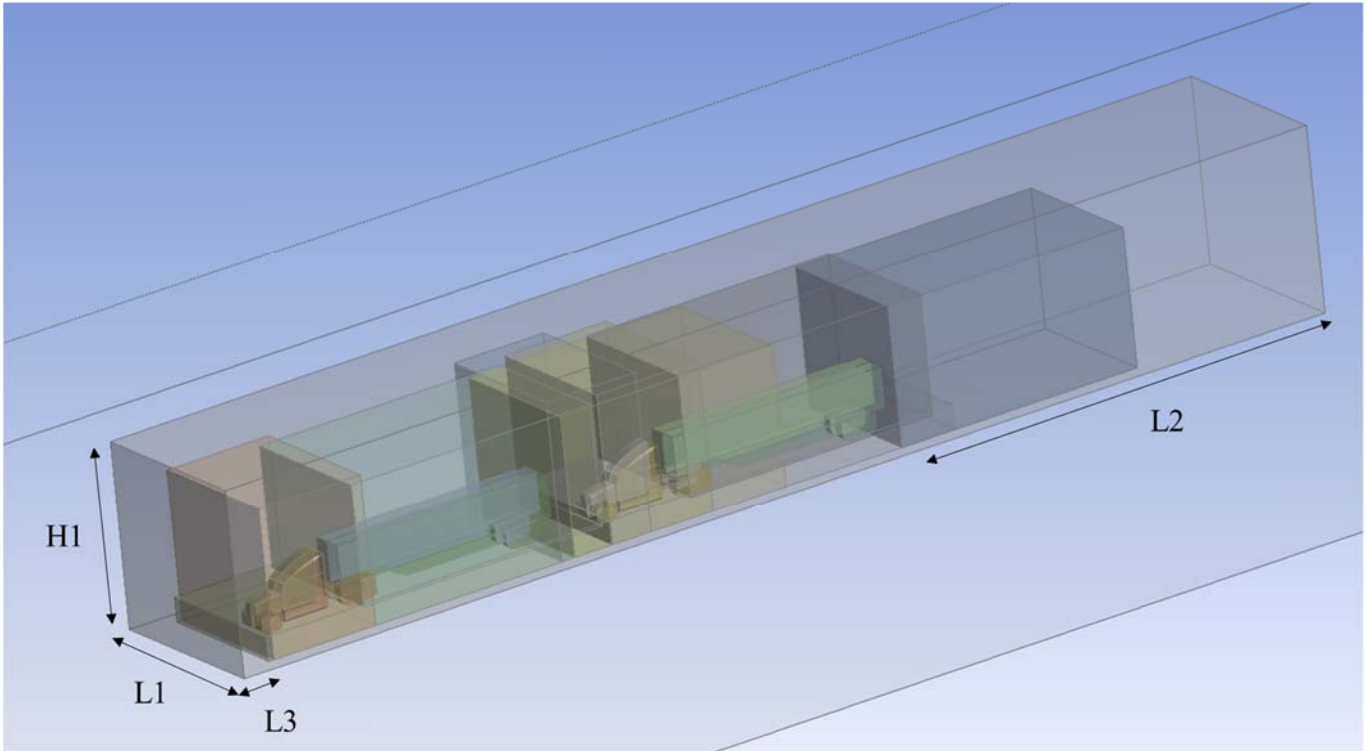
Figure 30: Schematic of Volumetric Refinement Regions for Offset Trucks

Table 5-1 shows the dimensions that correspond to Figure 30, which was held constant throughout the offset series, where again, L1 is the width of the box, L2 is the length from the rear surface of the follower trailer to the edge of the refinement zone, L3 is the length from the refinement zone to the front surface of the lead truck, and H1 is the height of the refinement zone.

Table 5-1: Refinement Region Dimensions

L1	= 300 inches
L2	= 1200 inches
L3	= 200 inches
H1	= 500 inches

The only significant change to this large refinement region from the two truck non-offset simulations is the additional 50 inches of width added to the refinement region. This extra 50 inches of width is also included in each of the other interior volumetric refinements.

Additionally, to remain as consistent as possible during the analysis, the same solution parameters were implemented for the laterally offset cases. These are summarized once again in Table 5-2 for convenience.

Table 5-2: Summary of CFD solution parameters for lateral offset cases

Solution Methods	
Turbulence Model	Non-Transient RKE
Pressure-Velocity Coupling	Coupled
Pressure Solution Method	Standard
Momentum Solution Method	SOU
Turbulent Kinetic Energy	SOU
Turbulent Dissipation Rate	SOU
Relaxation Factors	
Courant Number	50
Momentum Relaxation Factor	0.25
Pressure Relaxation Factor	0.25
Density Relaxation Factor	1
Body Forces Relaxation Factor	1
Turbulent Kinetic Energy Relaxation Factor	0.8
Turbulent Dissipation Rate Relaxation Factor	0.8
Turbulent Viscosity Relaxation Factor	0.8

Boundary Conditions	
Velocity Magnitude Inlet Condition	30 m/s
Pressure Outlet Condition	0 Pa Gauge Pressure
Turbulence Model Parameters	
Type	Realizable k-ε
C2-Epsilon	1.9
TKE Prandtl Number	1
TDR Prandtl Number	1.2
Wall- Treatment	Non-Equilibrium Wall Treatment

5.2 Results for Laterally offset simulations

After completing the CFD simulations, the converged coefficient of drag was then taken and normalized by the single truck coefficient of drag, of 0.5252, which was the same as during the non-laterally offset case. The results for the normalized coefficient of drag for the laterally offset cases are presented in Figure 31. Additionally, a comparison to the non-offset case, and the most extreme 2ft. lateral offset case are shown in Figure 32, as an extreme example to shown how the trend changes as the lateral offset increases.
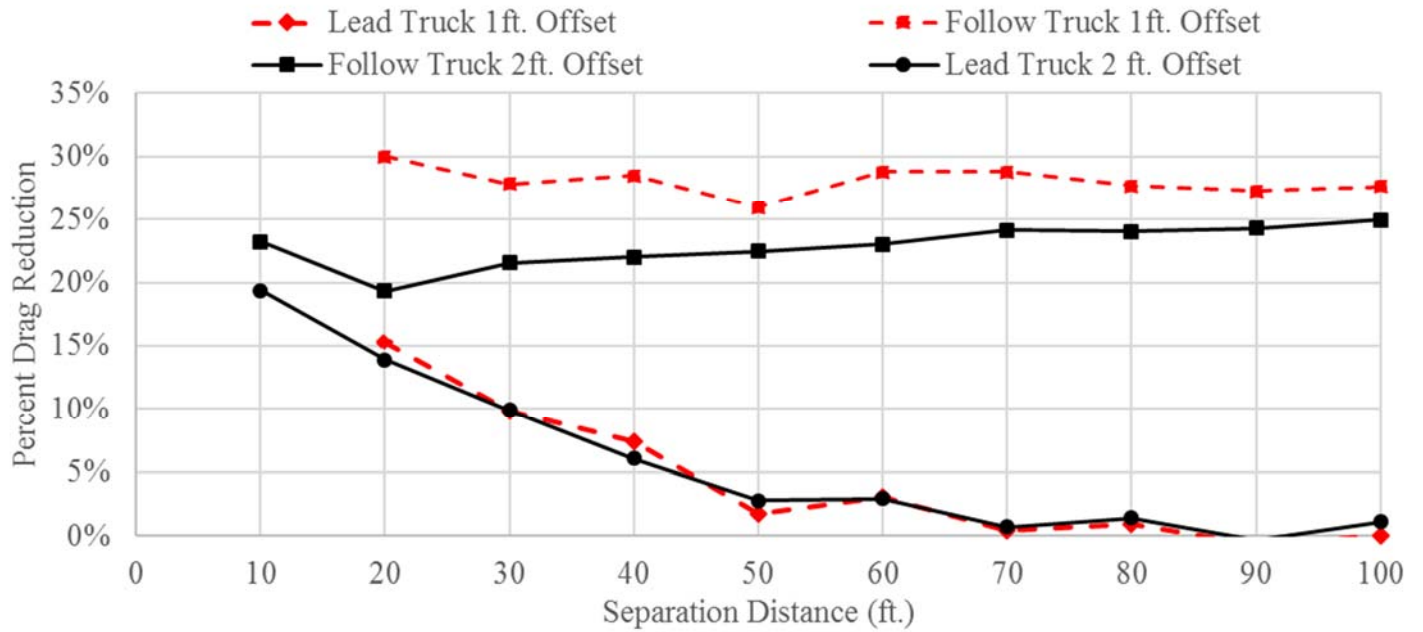
*Figure 31: Percent drag reduction vs. separation distance compared for 1ft. offset and 2 ft. offset*
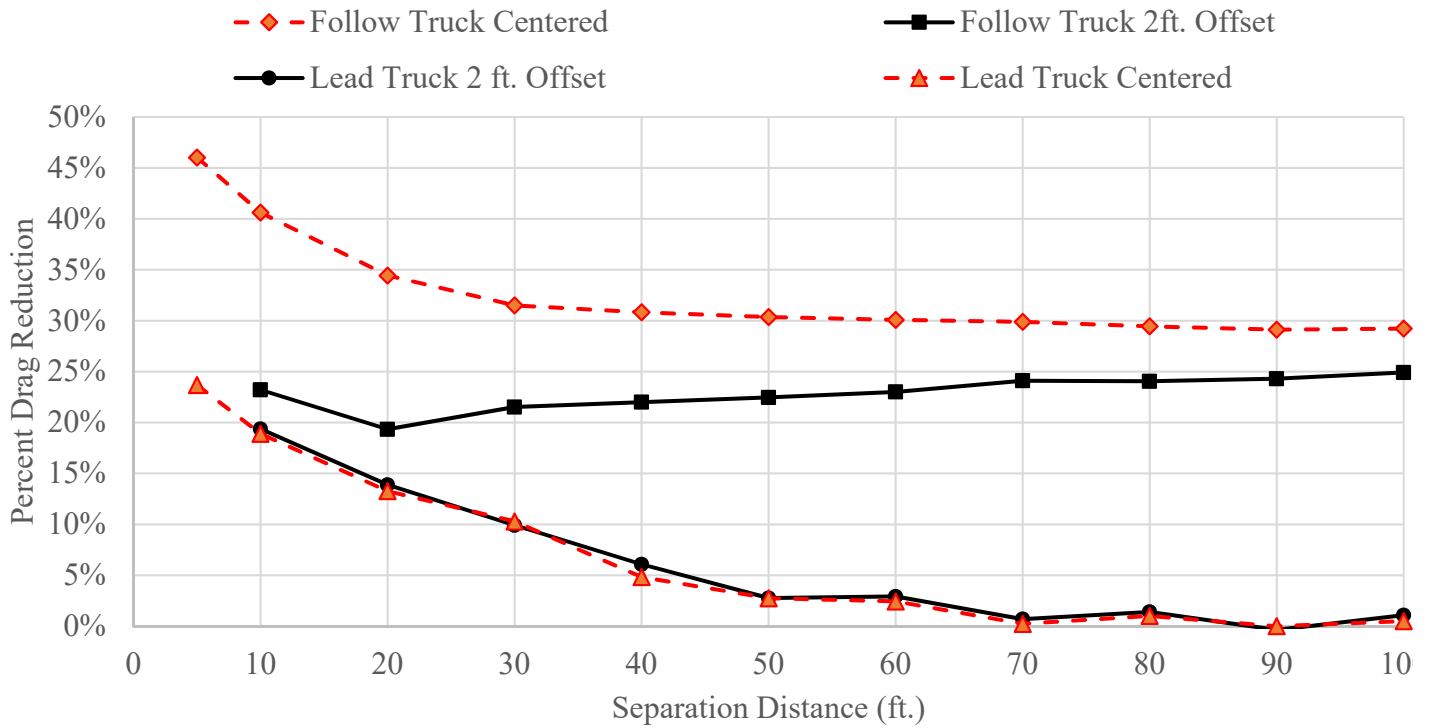
Figure 32: Percent drag reduction vs. separation distance comparison for non-offset and 2ft. offset

Figure 32 shows the large difference in the follower truck's drag reduction vs. separation distance. Interestingly, the follower truck performs significantly worse than the centered case while the lead truck performs very similarly to the centered case. In terms of the mechanisms for the drag reduction, the patterns fit what one would intuitively expect from offsetting the vehicles. The follower truck experiences drag reduction via "slipstreaming" in the wake of the lead vehicle. However, the extremely low velocity region behind the lead truck is relatively narrow in the lateral direction, as shown in Figure 33. Therefore, a portion of the front truck is then exposed to the higher-velocity air of the freestream which, while centered, is normally protected via the lead truck's wake. This results in an increased stagnation pressure on the front surface of the follower truck.
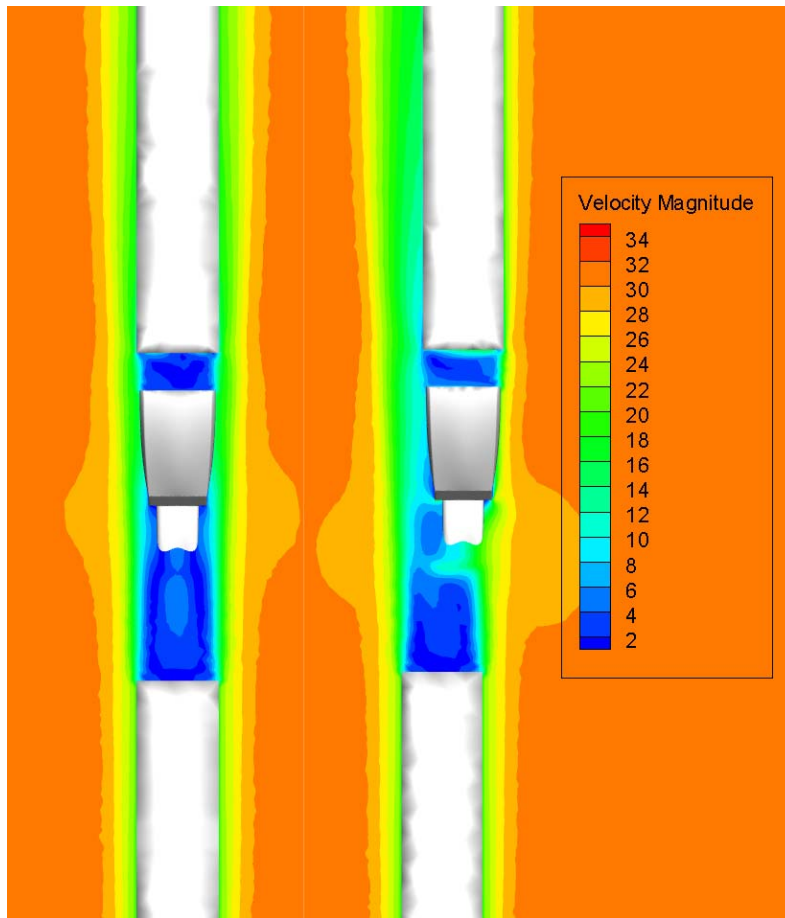

Figure 33: Top view of wake structure for offset and non-offset case at 10 ft. separation distance

Figure 34 shows the pressure contour on the front surface of the follower truck at 10 ft. separation distance for the centered case versus the 2ft. lateral offset case. Examining this figure shows that the pressure acting on the front surface of the vehicle changes dramatically in the offset case for the front surface of the follower vehicle. In the offset case, the pressure changes from a symmetric, relatively low distribution to an asymmetrical distribution, where the portion of the vehicle exposed to the free-stream flow sees a much higher pressure, nearly 350 Pa versus the 215 Pa maximum experienced in the centered case.
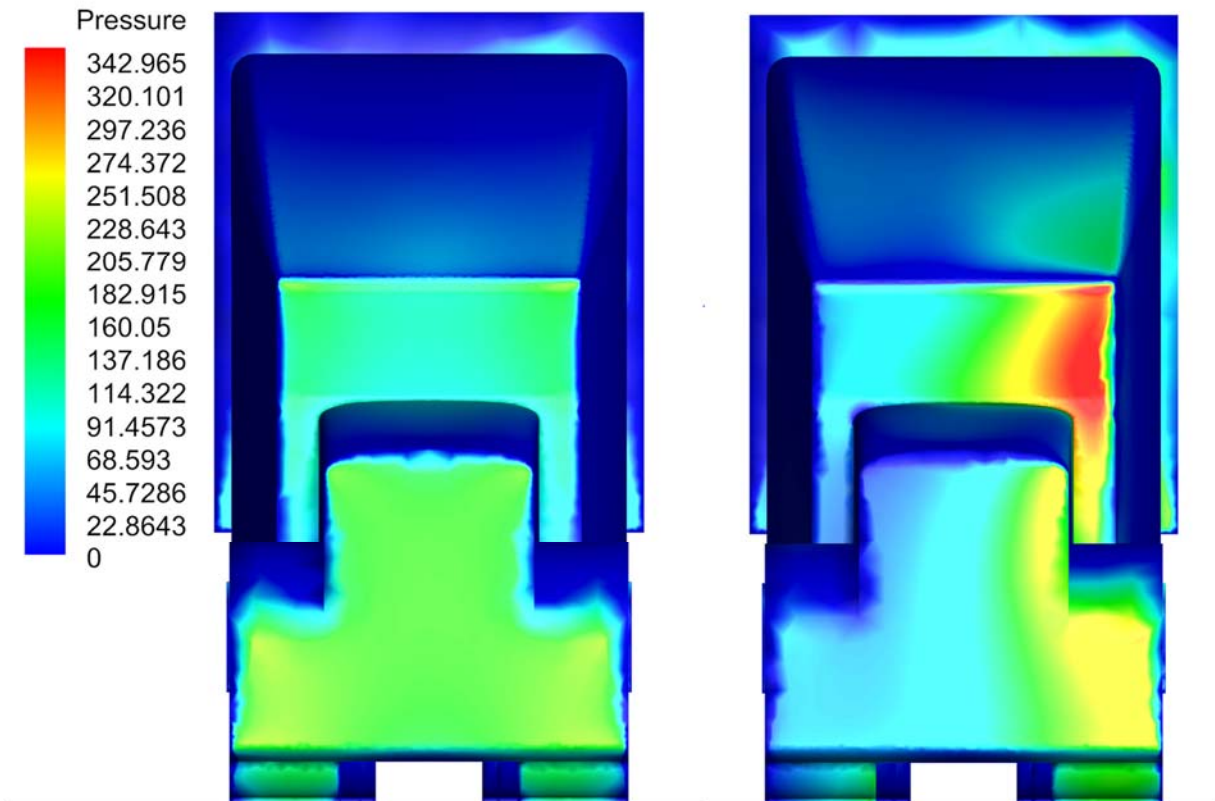
Figure 34: Pressure contour on the front surface of follower truck for centered case vs. 2ft. lateral offset case (10ft. separation distance, units in Pa)

In terms of the operation of the platoon however, this asymmetricity of the pressure distribution tends to try to force the follower vehicle back into the wake, thereby lessening the effect this trend has in general operation. The higher the asymmetrical pressure distribution, the

larger the force pushing the follower vehicle back into the wake becomes. This results in the vehicles tending to naturally self-correct in operation.

In contrast to the follower truck, the lead truck typically experiences drag reduction through an increase in pressure on the rear surface of the trailer. Even at close distances, most of the follower vehicle still lies within the low-pressure region behind the lead vehicle, and thus the difference in this pressure profile is slight, as shown in Figure 35. Therefore, the mechanism for which the lead vehicle receives drag reduction is barely impacted via the introduction of a lateral offset, even in a relatively extreme case of 2 ft. lateral offset. This results in an extremely similar trend to that of the centered case for the lead vehicle.
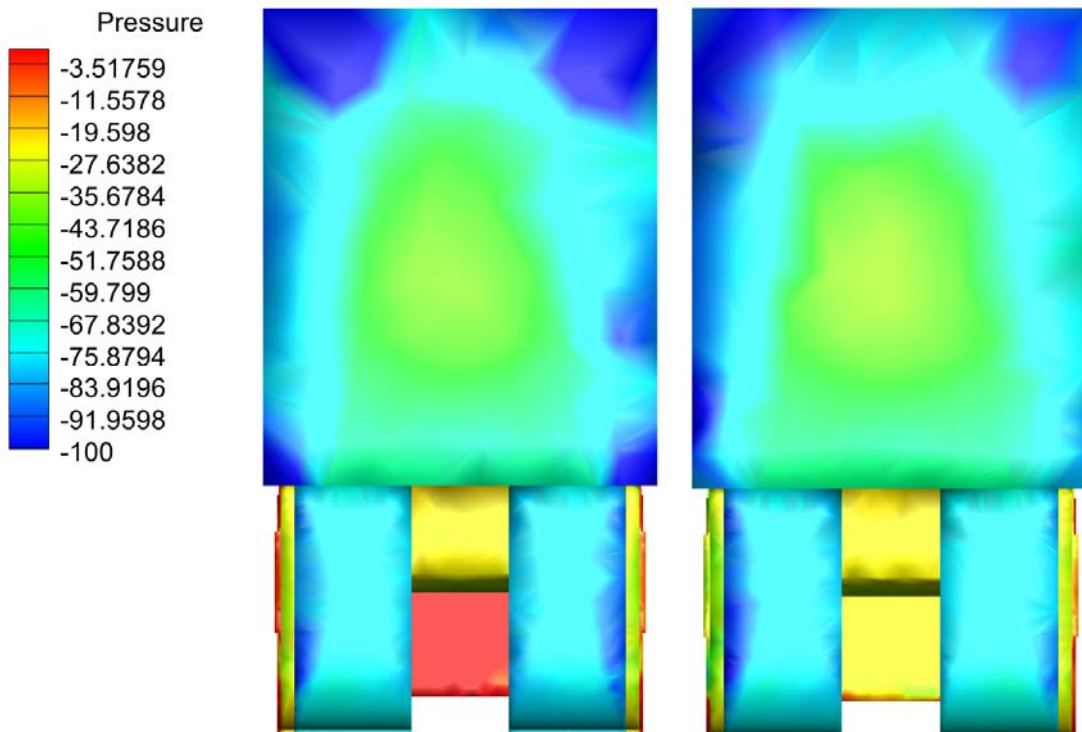

Figure 35: Pressure contour on the rear surface of the lead truck for centered case vs. 2 ft. lateral offset case (10 ft. separation distance, units in Pa)

While the results are very striking for the extreme case of a 2-ft. lateral offset, the impact of offsetting the follower truck can be seen even at comparatively small offsets. Figure 36 shows the results from a second set of simulations conducted at a reduced set of close separation distances at a lateral offset of 8 inches. Even at only 8 inches, the follower vehicle sees a 4% loss in drag reduction from the centered case, which rapidly diminishes as the separation distance increases. While the small percentage loss may seem insignificant, even a small decrease in the fuel savings can result in large ramifications over the large number of miles vehicles equipped with DATP technologies travel.
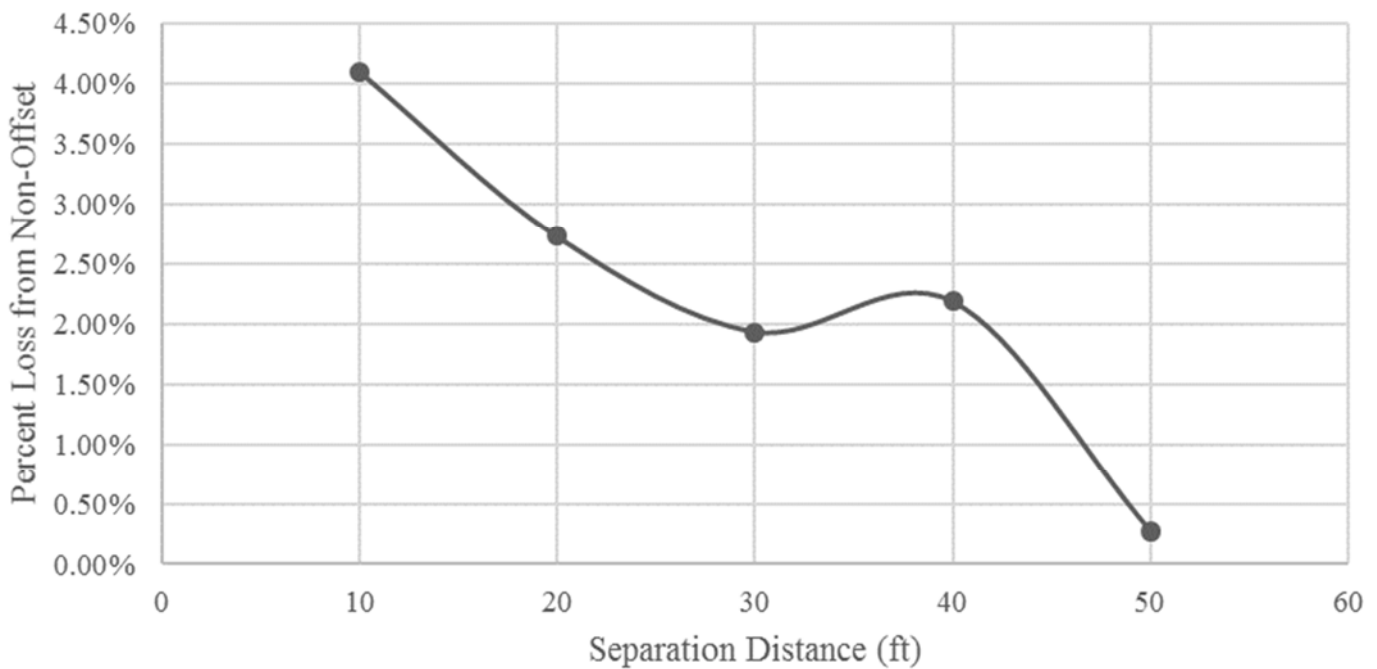
Figure 36: Percent loss of 8-inch offset compared to centered follower vehicle vs. separation distance

After investigation into the lateral offset, it is possible that lateral offset may degrade the performance of a DATP system. A small number of groups have investigated the impact of external variables, such as crosswind, on generic bluff bodies. DATP systems inherently change the

aerodynamics of the platoon, increasing various dependences on external variables. Therefore, crosswind may play an even more important role in a platooning system as the individual aerodynamic dependence is then coupled with the effects of platooning. The next chapter then describes an initial effort to quantify the effects of crosswind on a DATP system.

Chapter 6

Analysis of Crosswinds on Drag Reduction

There have been a small number of studies which investigate the impact of ambient variables such as crosswind on the aerodynamic performance of platooning vehicles [41,42]. Additionally, in Gheyssens, the effect of crosswind on a bluff body platoon was investigated. Gheyssens found that the crosswind has little effect on the overall platoon, or at best it increased the effectiveness of the platoon, concluding that the effect was linked most closely to the frontal radius of the bodies involved in the platoon [42].

In this chapter, the centered two-truck platoon was modeled with crosswind, rather than a generic bluff body. In addition, the crosswind's interaction with a lateral offset is also investigated, and the results are compared to the centered two-truck platooning results.

6.1 Crosswind simulation setup

Similar to the other simulation efforts, most of the meshing and solution parameters remained constant to ensure a consistent modeling effort throughout this thesis. The volumetric and surface refinements remained the same for the crosswind case, and the bounding box was deemed sufficiently wide enough to ensure a zero-gauge pressure outlet condition along sidewall of the bounding box.

To implement the crosswind within the simulation, the boundary conditions on the bounding box were changed. The velocity-inlet's definition at the front of the bounding box was changed from a magnitude normal to the boundary to being component defined. Additionally, one sidewall of the bounding box was changed to a velocity-inlet defined via components, and the opposite sidewall was updated to become a pressure-outlet with a zero-gauge pressure condition. For all the

crosswind simulations, the frontal velocity remained 65 mph or 29.0576 m/s, and the crosswind was simulated at 5 mph or 2.2352 m/s. Table 6-1 summarizes these inlet conditions. Establishing two inlet surfaces with component velocities helps to ensure a uniform flow-field in the far-field impinging on the platoon, without creating the problematic boundary conditions at the interface of the two surfaces.

Table 6-1: Crosswind inlet conditions for favorable offset

Direction	Velocity
Front Surface	
X-velocity	2.2352
Y-Velocity	0
Z-Velocity	-29.0576
Left Surface	
X-velocity	2.2352 m/s
Y-Velocity	0
Z-Velocity	-29.0576 m/s

6.2 Crosswind Results

To remain consistent in the calculation of the percent drag reduction, a new baseline single truck simulation was conducted with a 5-mph crosswind. This resulted in a coefficient of drag value of 0.6481 for a single truck that was then used as the baseline for the remainder of the crosswind simulations for the purposes of calculating the percent drag reduction, where the calculation was shown previously in Equation. (3.3).

6.2.1 Crosswind Platoon vs. Separation Distance Results

Once the baseline simulation was complete, a series of simulations at the same separation distances as the previous simulation series were conducted. The results, presented as percent drag reduction are shown in Figure 37.

The drag reduction versus separation distance trend for the 5-mph crosswind is much less smooth than the than the centered cases without crosswind. Despite the higher irregularity, it follows the same general trend. In general, the percent drag reduction increases as the separation distance diminishes. The smoothness may be attributed to the turbulence model, and the choice to not make the simulations time-resolved. Since the vortex shedding off of the vehicles is generally asymmetrical in both time and space, a steady-state solution may not fully capture some of the time-dependent effects that would be captured using a time-averaged solution.
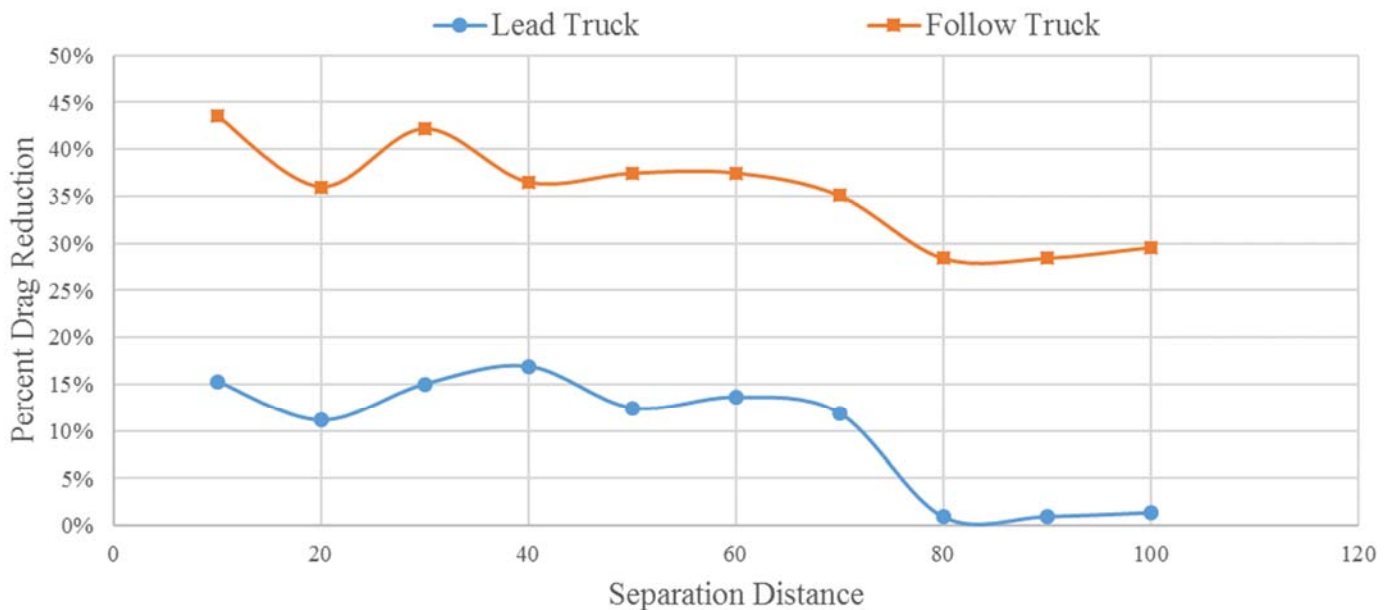

Figure 37: Drag reduction vs. separation distance for centered 5mph crosswind

6.2.2 Crosswind Laterally Offset Platoon vs. Separation Distance Results

After comparing a series of baseline testing, the next step was to understand how the drag reduction responded to the combination of both the lateral offset and the crosswind. Additionally, the direction of the crosswind could have a significant impact on the drag experienced from each vehicle. Therefore, two different directions were considered, one with the crosswind in coming from the direction of the lateral offset, which for convenience is simply labeled standard, and one where the direction of the wind comes from the opposite side, termed the opposite crosswind.
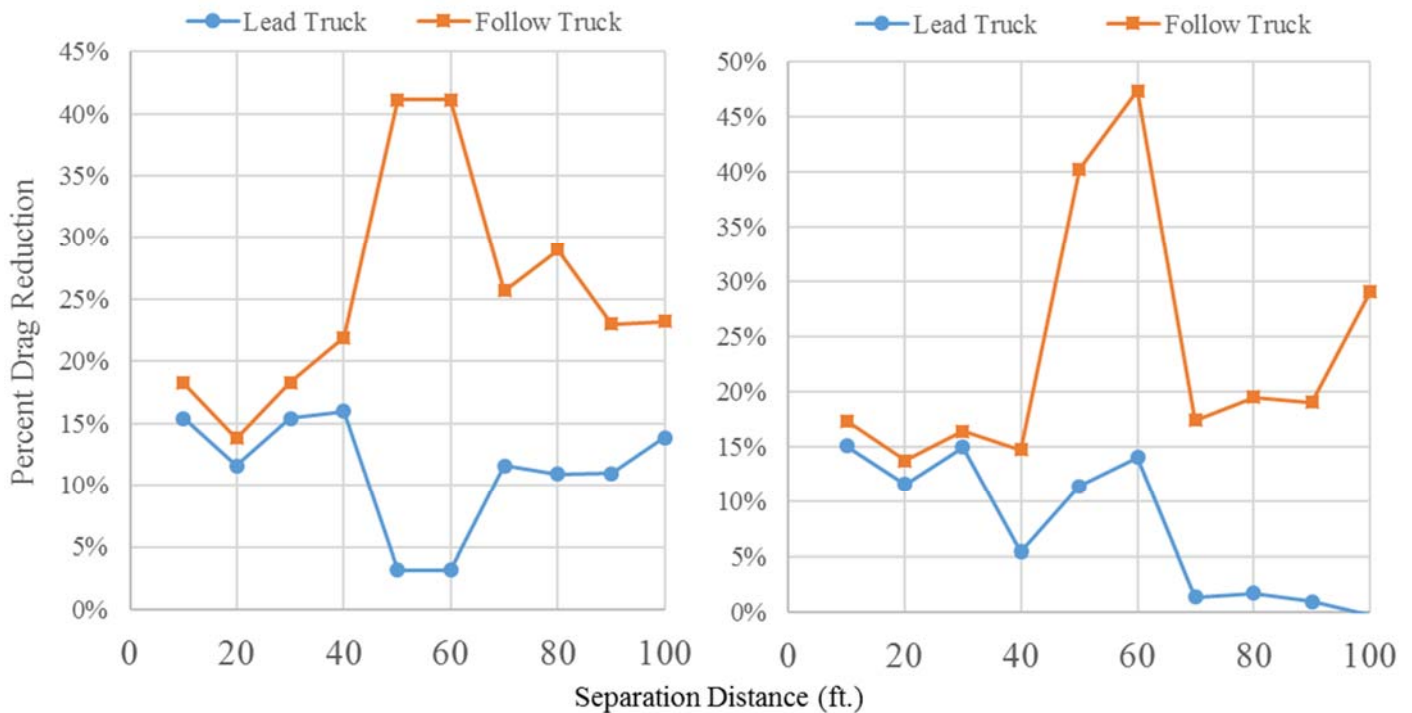
Figure 38: Drag reduction vs. separation distance for 2ft. laterally offset, 5mph crosswinds, (left)standard crosswind, (right) opposite crosswind

The simulations with crosswind and offset are shown in Figure 38 and present a very different trend from those of the offset without any crosswind. The significantly large peak at 50-60 feet separation distance are not exhibited in any of the other trends developed previously. The follower truck sees a sharp gain in percent drag reduction at this distance. Examining the wake

structure at this separation distance provides some insight into why a local maximum occurs at this separation distance. Figure 39 compares the velocity magnitude for three various simulations, to show the wake structure of the vehicles.
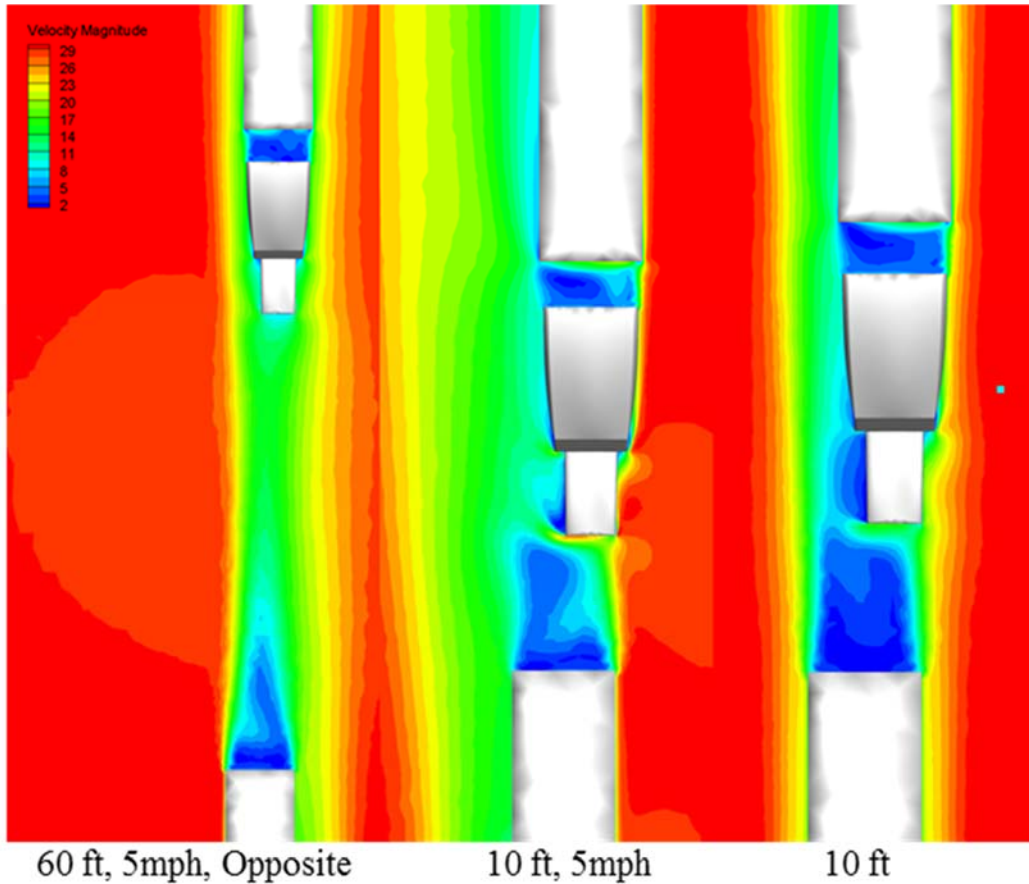
Figure 39: Comparison of velocity magnitude slices showing the wake structure surrounding platoon

From Figure 39, it is clear that the crosswind is extending the wake of the lead vehicle in the direction of the crosswind. Additionally, the crosswind appears to be affecting the development of the low-pressure region behind the lead truck, increasing the pressure as well as the velocity developing in the wake immediately behind the lead truck. This results in a significant falloff of the follower truck's benefits, while maintaining the lead truck's gains.

Figure 40 then shows the pressure distribution that arises on the front surface of the follower vehicle. Once again, at low separation distances, the effect of being laterally offset is

significantly more pronounced. The pressure contour on the far-right image represents the 2ft. lateral offset case without the crosswind. Without the crosswind, there is an asymmetrical high pressure distribution on the side of the cab that is exposed to the freestream flow. As mentioned in Chapter 5, this realized pressure is significantly higher than that of the non-offset follower truck. The middle image demonstrates the effect of the crosswind on the offset case. At the close separation distances, the crosswind accentuates the asymmetrical high pressure distribution of the lateral offset.

| a) 50ft, 2ft offset, 5mph crosswind | b) 10ft, 2ft offset, 5mph crosswind | c) 10ft, 2ft offset, no crosswind |
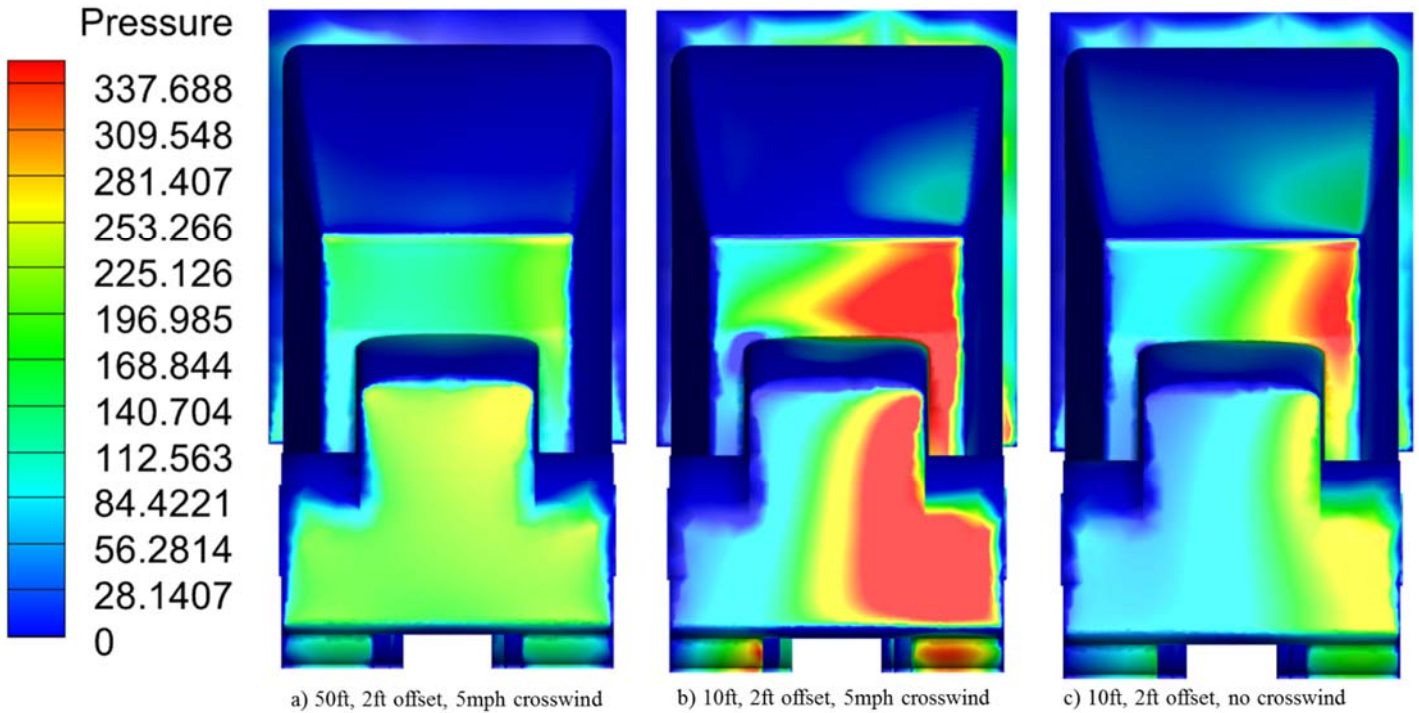
Figure 40: Comparison of pressure contours on the front surface of the follower truck

One possible explanation for the extreme difference between the offset's crosswind drag coefficient is a resonant behavior between the crosswind and the offset. At selected distances, the crosswind couples with the offset's influence on the wake, specifically the vortices being shed on the lead vehicle. Since the vortices are shed asymmetrically, and are time-dependent, the steady-

81

state solution may be representing only a case where the mean flow and vortex shedding couple with the crosswind in an anti-resonance to diminish the negative impact of the lateral offset. However, at other separation distances, the crosswind amplifies the mean flow, as well as strengthens the vortices, rather than weakening them, which results in the large differences in pressure realized on the front surface of the follower vehicle. Since the simulations are not-time resolved, and the wake structures may not be realistically modeled using the RKE solution, further work should be conducted to determine the accuracy of the effect cross has on platooning.

Chapter 7

Conclusions and Future Work

7.1 Conclusions

The goal of the this thesis was to investigate the drag reduction trend of two trucks in a Driver Assistive Truck Platooning (DATP) system. The overall conclusion was that the drag reduction for the overall platoon increased as the separation distance diminished. This was evident for all scenarios tested. In the initial platooning simulations, both vehicles' drag reduction increased as the separation distance decreased, which matched the previous general consensus of previous research.

The experimental fuel economy testing conducted in Chapter 5 showed the same result for the combined platoon, but the follower truck exhibited a local maximum at a separation distance of 50 feet, rather than the monotonic trend predicted by the original CFD simulations. This prompted an investigation into the various factors that might contribute to a degraded fuel economy trend at the close separation distances. Temperature control and throttle dither were investigated to ensure that these factors were not a significant contribution to the degradation of the fuel economy trend.

Lateral offset was identified as one of the potential culprits for the degrade trend. A second set of simulations was conducted to investigate the effect of lateral offset on the drag reduction. These results showed a degraded trend for the follower vehicle at separation distances closer than 40 ft, while the lead vehicle retained its drag reduction. Therefore, the combined overall truck platooning trend matched much closer to the experimental fuel economy results. The asymmetrical pressure distribution caused by the lateral offset also tends to return the offset

follower vehicle to the centered case, as the pressure rises on the laterally offset side. Thus, while the drag reduction of the platoon may be enhanced by adding lateral control, the truck platoon tends to naturally self-correct the lateral offset introduced by steering errors. This may limit the need for enhanced lateral control to see high effectiveness on platooning systems. However, if future DATP systems employ close spacings, lateral steering may be beneficial to ensure maximized fuel efficiency.

Additionally, the impact of a small crosswind was investigated, especially in regards to its combination with lateral offset. The CFD results from the crosswind show that for the centered case, the crosswind simply reduces the drag reduction from both vehicles, as it alters the wake behind the lead vehicle. When coupled with lateral offset however, the crosswind enhances the degradation of the follower truck trend at close distances. At the larger distances, however, the crosswind appears to help mitigate the degradation caused by the lateral offset.

Overall, DATP systems promise large drag reduction, and thus increased fuel economy for both vehicles in the platoon. Given the extremely large numbers of miles travelled in the United States by heavy vehicles, DATP technology represents a promising new avenue to increase safety for heavy vehicles while reducing both fuel consumption and the emissions associated with transportation.

7.2 Future Work

While significant work has been conducted both in this thesis and in other research, there are still large areas that still require additional investigation. One major area of improvement for CFD analysis done in this thesis would be to shift towards a fully time-resolved solution. Many of the investigated phenomenon are time-dependent, which a steady-state solution may not accurately

represent. A time-averaged solution may alleviate some of the inaccuracies present with a steady-state solution. In the same fashion, a higher fidelity turbulence model may reveal some of the underlying physics causing many of the interactions.

Recently, there has been some research which suggests that even without lateral offset, the CFD simulations which predict monotonic drag reduction as the separation distance diminishes may not fully capture the aerodynamic trends regarding the vehicle [Citation, Kevin's Suggestions with Wind Tunnels]. This gives rise to the idea that there may be additional aerodynamic effects that were not investigated in this work or the previous work related to two truck platooning which may be negatively influencing the platoon's drag reduction trend at the close separation distance. This may be a result of the limited scope of varied parameters in the conducted study. Previous research has suggested that the aerodynamics surrounding heavy vehicles has many complex interactions, many of which were simplified in order to characterize the drag reduction trend in regard to separation distance. Uniformity amongst the tested parameters, whilst allowing comparisons, may also have hidden some of the complex interactions, e.g. how the geometry of the side skirts, or the trailer gap, may have on platooning, and how it might influence the drag reduction trend.

Additionally, investigating other parameters that have a large effect on the performance on isolated trucks, and how they interact within platooning investigations would be beneficial. Geometric parameters such as the trailer gap or aerodynamic additions such as boat-tails or fairings have a large impact on the drag characteristics of tractor-trailer vehicles. Given the complicated interaction between the separation distance and the two vortices that develop in the follower truck's trailer gap may be heavily influenced by platooning the vehicles, and thus represents an area of high interest.

Additionally, different geometries, such as flatbed trailers, tankers, or even alternative European cab-over style geometries and their interactions with platooning systems is an under-represented area of research interest. Given that these areas are also high-risk in terms of operator safety, automation in these industries represents an additional aspect of interest for the industry.

Finally, very little work has been conducted on larger platoons. Platoons of four or more vehicles may be sufficient to confirm a generally held hypothesis, including the previous work conducted, that in larger platoons the interior vehicles see additional drag reduction when compared to the exterior vehicles. Since large fleets owned by singular companies are likely to be first adopters of DATP technologies, it is highly likely that there is a desire for vehicles to be in larger than two or even three truck platoons. Thus, performance of vehicles in large platoons would be beneficial.

References

1.   SelectUSA, "Logistics and Transportation Spotlight," URL: https://www.selectusa.gov /logistics-and-transportation-industry-united-states, Accessed: Apr. 2017

2.   Federal Highway Administration "Freight Analsysis Framework," URL: https://ops.fhwa.dot.gov/freight/freight_analysis/faf/, Accessed: Apr. 2017

3.   Torrey IV, W.F. (ATRI) and Murray, D. (ATRI), "An Analysis of the Operational Costs of Trucking: A 2014 Update," 36, http://www.atri-online.org/wp-content/uploads/2014/09/ATRI-Operational-Costs-of-Trucking-2014-FINAL.pdf, 2014. Accessed: Apr. 2017

4.   U.S. Energy Information Administration, "Petroleum & Other Liquids," 2015–2016, http://www.eia.gov/dnav/pet/pet_cons_wpsup_k_4.htm%5Cnhttp://www.eia.gov/dnav/pet /PET_PNP_PCT_DC_NUS_PCT_A.htm, 2016. Accessed: Apr. 2017

5.   Ortega, J., Dunn, T., McCallen, R., and Salari, K., "Computational Simulation of a Heavy Vehicle Trailer Wake," Aerodynanmics of Heavy Vehicles, Trucks, Buses, and Trains 19:219–233, 2004, doi:10.1007/978-3-540-44419-0_22.

6.   Hucho, W.-H. and Aerodynamik., "Aerodynamics of Road Vehicles: From Fluid Mechanics to Vehicle Engineering," (Amsterdam, Elselvier Ltd., 1987), ISBN: 9780750612678

7.   Walmart Inc., "Walmart Debuts Futuristic Truck," URL: http://corporate.walmart.com /_news_ /news-archive/2014/03/26/walmart-debuts-futuristic-truck, Accessed: Apr 2017

8.   Department of Energy, "SuperTruck Making Leaps in Fuel Efficiency," URL: http://energy.gov/eere/articles/supertruck-making-leaps-fuel-efficiency. Acccessed: Apr 2017

9.   McAuliffe, B.R. and Wall, A.S., "Aerodynamic Performance of Flat-Panel Boat-Tails and Their Interactive Benefits with Side-Skirts," SAE International Journal of Commercial Vehicles 9:70–82, 2016, doi:10.4271/2016-01-8015.

10. McGehee, D. V., Mazzae, E.N., and Baldwin, S.G.H., "Driver reaction time in crash avoidance research: Validation of a driving simulator study on a test track," Proceedings of the 44th Annual Meeting of Humam Factors and Ergonomics Society 320–323, 2000, doi:10.1177/154193120004402026.

11. Federal Highway Administration "Title 23 Code of Federal Regulations Part 658.17." URL: https://www.fhwa.dot.gov/legsregs/directives/fapg/cfr0658b.htm, Accessed: Apr 2017

12. Agogino, A., Goebel, K., and Alag, S., "Intelligent sensor validation and sensor fusion for reliability and safety enhancement in vehicle control," Inst. Transport. Studies, Univ. California, Berkeley, California PATH Res. Rep. UCB-ITSPRR-95-40, 1995, URL: http://www.path.berkeley.edu/sites/default/ files/publications/PRR-95-40.pdf, Accessed: Apr 2017.

13. SAE International Surface Vehicle Recommended Practice, "Taxonomy and Definitions for Terms Related to On-Road Motor Vehicle Automated Driving Systems", SAE Standard J3016, Rev. Jan. 2014

14. Federal Highway Administration, "Federal Highway Adminstration No. DTFH61-13-R-00011 Exploratory Advanced Research Program," https://www.fbo.gov /index?s=opportunity& mode=form&id=70cff813a8c898c9f4e53a023f284a2f&tab=co re&_cview=1, Accessed: Apr. 2017

15. Watts, A., "Computational Characterization of Drag Reduction for Platooning Heavy Vehicles," Masters Thesis, Aerospace Engineering Department, Auburn University, 2015.

16. Barlow, J.B., Rae, W.H., and Pope, A., "Low-Speed Wind Tunnel Testing," (New York, John Wiley and Sons Inc. 1999). ISBN: 978-0471557746

17. Turner, T.R., "Wind-Tunnel Investigation of a 3/8-Scale Automobile Model Over a Moving-Belt Ground Plane," NASA Tech. Note, 1967

18. ANSYS Inc., "ANSYS FLUENT," URL: http://www.ansys.com/Products/Fluids/ANSYS-Fluent, Accessed: Apr. 2017

19. SAE International Surface Vehicle Recommended Practice, "Fuel Consumption Test Procedure - Type II," SAE Standard J1321, Rev. Feb. 2012.

20.   Ahmed, S., Ramm, G., and Faltin, G., "Some Salient Features Of The Time-Averaged Ground Vehicle Wake," SAE Technical Paper 840300, 1984, doi:10.4271/840300

21.   Khan, R.S. and Umale, S., "CFD Aerodynamic Analysis of Ahmed Body," Int. J. Eng. Trends Technol. 18(7):301–308, 2014. ISSN:2231-5381.

22.   Liu, Y. and Moser, A., "Numerical modeling of airflow over the Ahmed body," Proceeding 11th Annual Conferemce of the CFD Society, Canada 508–513, 2003.

23.   Pagliarella, R., Watkins, S., and Tempia, A., "Aerodynamic Performance of Vehicles in Platoons: The Influence of Backlight Angles," SAE Technical Paper 2007-01-1547, 2007, doi:10.4271/2007-01-1547.

24.   Pagliarella, R., Watkins, S., and Tempia, A., "Aerodynamic Performance of Vehicles in Platoons: The Influence of Backlight Angles," SAE Technical Paper 2007-01-1547, 2007, doi:10.4271/2007-01-1547.

25.   Yoshida, J., Sugimachi, T., Fukao, Y., and Suzuki, Y., "Autonomous Driving of a Truck Based on Path following Control," presented at 10th Int. Symposium on Advanced Vehicle Control,UK, August 22-26, 2010.

26.   Browand, F., McArthur, J., and Radovich, C., "Fuel Saving Achieved in the Field Test of Two Tandem Trucks," 2004 USC, UCB-ITS-PRR-2004-20.

27.   Lammert, M.P., Duran, A., Diez, J., Burton, K., and Nicholson, A., "Effect of Platooning on Fuel Consumption of Class 8 Vehicles Over a Range of Speeds, Following Distances, and Mass," SAE Int. J. 14, 2014, doi:10.4271/2014-01-2438.

28.   Peloton Technology Inc., "Peloton Technology," URL: http://peloton-tech.com/, Accessed: Apr. 2017

29.   Dassault Systems, "3-D CAD Design Software," URL: http://www.solidworks.com/, 2017, Accessed: Apr. 2017.

30.   Dassault Systems "SAE Design and Analysis Project with SolidWorks Software," 186. URL:

31. ANSYS Inc., "FLUENT Theory Guide," http://www.afs.enea.it/project/neptunius/docs/fluent/html/th/main_pre.htm , Accessed: Apr. 2017

32. Launder, B.E., Spalding, D., "The Numerical Computation of Turbulent Flows," Computational Methods in Applied Mechanics and Engineering 3.:269–289, 1974.

33. Hinze, J.O., "Turbulence," (New York, McGraw-Hill Publishing Co., 1975) ISBN: 978-0070290372

34. Kim, S.. and Choudhury, D., "A Near-Wall Treatment Using Wall functions Sensitized to Pressure Gradient," ASME 1995.

35. Hinterberger, C., Garcia-Villalba, M., and Rodi, W., "Large Eddy Simulation of Flow Around the Ahmed Body," Aerodynamics of Heavy Vehicles, Trucks. Buses and Trains, Vol. 1, 2004, doi:10.1016/j.ijheatfluidflow.2008.02.002.

36. Bayraktar, I., Landman, D., and Baysal, O., "Experimental and Computational Investigation of Ahmed Body for Ground Vehicle Aerodynamics," SAE Technical Paper, SAE Int., 2001, doi:10.4271/2001-01-2742.

37. Lanfrit, M., "Best practice guidelines for handling Automotive External Aerodynamics with FLUENT," URL : http://www.southampton.ac.uk/~nwb/lectures/ GoodPracticeCFD/Articles/Ext_Aero_Best_Practice_Ver1_2.pdf, Accessed: Apr. 2017

38. SAE International Surface Vehicle Recommended Practice, "Fuel Consumption Test Procedure - Type II," SAE Standard J1321, Rev. Oct. 1986.

39. Brown, L. and Schubert, R., "Discussions with team members", 2016.

40. Azim, A.F.A., "An Experimental Study of the Aerodynamic Interference Between Road Vehicles," SAE Technical Paper, SAE International, 1994, doi:10.4271/940422.

41. Gaudet, B., "Review of Cooperative Truck Platooning Systems," Technical Report, 2014, doi:10.1039/B910216G.

42.   Gheyssens, T., "Aerodynamic Analysis of a Platoon of Bluff Bodies Subjected to Cross Wind, a Numerical Investigation on the Effect of Drag Reduction Devices," Master's Thesis, Department of Aerospace Engineering, Delft University of Technology, 2016.